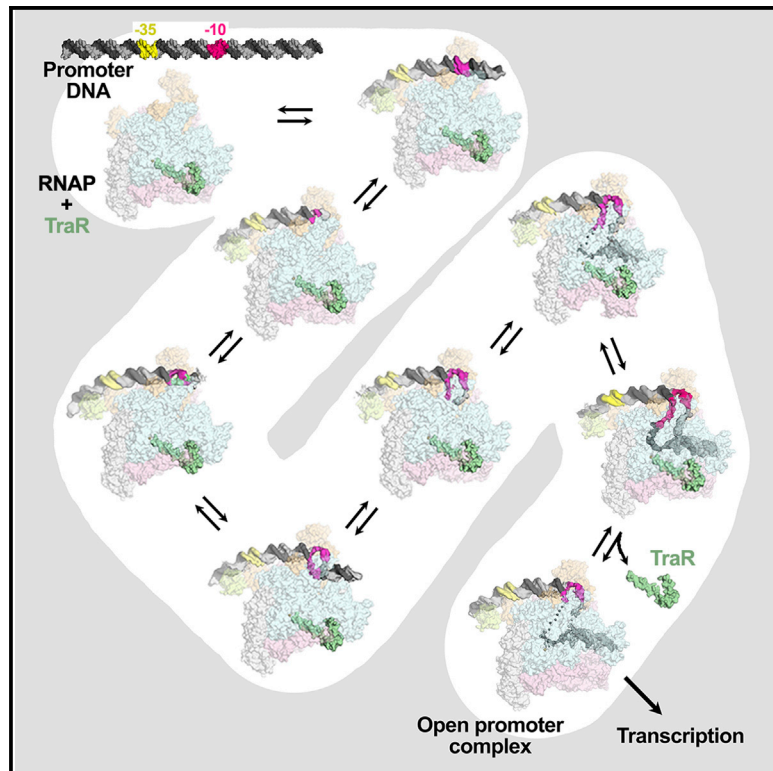


# Stepwise Promoter Melting by Bacterial RNA Polymerase

## Graphical Abstract



## Authors

James Chen, Courtney Chiu,  
Saumya Gopalkrishnan, ...,  
Richard L. Gourse,  
Elizabeth A. Campbell, Seth A. Darst

## Correspondence

darst@rockefeller.edu

## In Brief

Cryo-EM structures of RNA polymerase-promoter DNA intermediates identify stages in transcription initiation from the initial recognition of double-stranded promoter DNA in RPc to final promoter melting in RPo. Structural analyses of RNA polymerase and DNA conformational changes delineate steps in the pathway. Biochemical and genetic characterization support their functional importance.

## Highlights

- Cryo-EM structures of 7 intermediates in promoter opening pathway from RPc to RPo
- Intermediates populated by using an inhibitor and a promoter with unstable RPo
- RNAP and DNA conformational changes in mobile regions mark the steps in the pathway
- Transient interactions identified in intermediates are not found in RPc or RPo

# Stepwise Promoter Melting by Bacterial RNA Polymerase

James Chen,<sup>1</sup> Courtney Chiu,<sup>1</sup> Saumya Gopalkrishnan,<sup>2</sup> Albert Y. Chen,<sup>2</sup> Paul Dominic B. Olinares,<sup>3</sup> Ruth M. Saecker,<sup>1</sup> Jared T. Winkelman,<sup>2</sup> Michael F. Maloney,<sup>2</sup> Brian T. Chait,<sup>3</sup> Wilma Ross,<sup>2</sup> Richard L. Gourse,<sup>2</sup> Elizabeth A. Campbell,<sup>1</sup> and Seth A. Darst<sup>1,4,\*</sup>

<sup>1</sup>Laboratory of Molecular Biophysics, The Rockefeller University, New York, NY 10065, USA

<sup>2</sup>Department of Bacteriology, University of Wisconsin-Madison, Madison, WI 53706, USA

<sup>3</sup>Laboratory of Mass Spectrometry and Gaseous Ion Chemistry, The Rockefeller University, New York, NY 10065, USA

<sup>4</sup>Lead Contact

\*Correspondence: [darst@rockefeller.edu](mailto:darst@rockefeller.edu)

<https://doi.org/10.1016/j.molcel.2020.02.017>

## SUMMARY

Transcription initiation requires formation of the open promoter complex (R<sub>Po</sub>). To generate R<sub>Po</sub>, RNA polymerase (RNAP) unwinds the DNA duplex to form the transcription bubble and loads the DNA into the RNAP active site. R<sub>Po</sub> formation is a multi-step process with transient intermediates of unknown structure. We use single-particle cryoelectron microscopy to visualize seven intermediates containing *Escherichia coli* RNAP with the transcription factor TraR en route to forming R<sub>Po</sub>. The structures span the R<sub>Po</sub> formation pathway from initial recognition of the duplex promoter in a closed complex to the final R<sub>Po</sub>. The structures and supporting biochemical data define RNAP and promoter DNA conformational changes that delineate steps on the pathway, including previously undetected transient promoter-RNAP interactions that contribute to populating the intermediates but do not occur in R<sub>Po</sub>. Our work provides a structural basis for understanding R<sub>Po</sub> formation and its regulation, a major checkpoint in gene expression throughout evolution.

## INTRODUCTION

The transcription of cellular DNA cannot begin until RNA polymerase (RNAP) locates a promoter and forms the open promoter complex (R<sub>Po</sub>). In R<sub>Po</sub>, RNAP unwinds ~13 bp of DNA to form the transcription bubble and loads the template-strand (t-strand) DNA into the RNAP active site located within a deep cleft (Abascal-Palacios et al., 2018; Bae et al., 2015; He et al., 2016; Nagy et al., 2015; Plaschka et al., 2016; Tafur et al., 2016; Vorländer et al., 2018; Zuo and Steitz, 2015). The vast majority of initiation events in bacteria involve the RNAP catalytic core enzyme (termed E, subunit composition  $\alpha_2\beta\beta'\omega$ ) combined with the primary promoter specificity  $\sigma$  factor ( $\sigma^{70}$  in *Escherichia coli* [Eco]; Feklistov et al., 2014; Gruber and Gross, 2003), or E $\sigma^{70}$ . E $\sigma^{70}$  functions as a molecular isomerization machine, using

binding free energy to generate R<sub>Po</sub> through a multi-step pathway (Ruff et al., 2015).

Structures of bacterial R<sub>Po</sub> have been well characterized (Bae et al., 2015; Boyaci et al., 2019; Hubin et al., 2017b; Narayanan et al., 2018; Zuo and Steitz, 2015), but the structural basis for R<sub>Po</sub> formation is poorly understood due to the transient nature of intermediates along the pathway from initial E $\sigma^{70}$  recognition of the duplex promoter in the closed complex (R<sub>Pc</sub>) to the final R<sub>Po</sub> (Ruff et al., 2015). Previous kinetic analyses used salt, urea, and other perturbants to identify intermediates of R<sub>Po</sub> formation in solution (Gries et al., 2010; Kontur et al., 2008, 2010). Here, we used single-particle cryoelectron microscopy (cryo-EM) to visualize R<sub>Po</sub> formation by *Eco* RNAP. To facilitate the visualization of intermediates, we added TraR, an F plasmid-encoded transcription factor, and used a promoter that is inhibited by TraR but forms stable intermediates, the S20 ribosomal protein promoter *rpsT* P2 (Lemke et al., 2011; Gopalkrishnan et al., 2017; Chen et al., 2019b). Like its homolog DksA, TraR binds directly to RNAP rather than to promoter DNA, regulating transcription initiation *in vitro* and *in vivo* by increasing the occupancy of intermediates on the pathway (Blankschien et al., 2009; Gopalkrishnan et al., 2017; Chen et al., 2019b).

Using image classification approaches, we visualized 5 intermediates formed by the wild-type (WT) *rpsT* P2 promoter, and 2 additional intermediates formed by a mutant *rpsT* P2 promoter. Our structures span the R<sub>Po</sub> formation pathway from R<sub>Pc</sub> to R<sub>Po</sub> (Chen et al., 2019b). Features of the structures allow their placement in an ordered pathway that provides a structural basis for understanding R<sub>Po</sub> formation in all organisms.

## RESULTS

### TraR Stabilizes a Partially Melted Intermediate on the *rpsT* P2 Promoter

Our initial studies focused on E $\sigma^{70}$  complexes with the well-characterized *rnnB* P1 promoter, which forms an unstable R<sub>Po</sub> in the absence of initiating nucleotide triphosphates (NTPs) that is in rapid equilibrium with earlier intermediates (Gourse et al., 2018; Rutherford et al., 2009). However, we could not detect TraR-E $\sigma^{70}$ -*rnnB* P1 complexes by native mass spectrometry (nMS) or by cryo-EM, suggesting that these complexes were too unstable under cryo-EM conditions (Chen et al., 2019a).

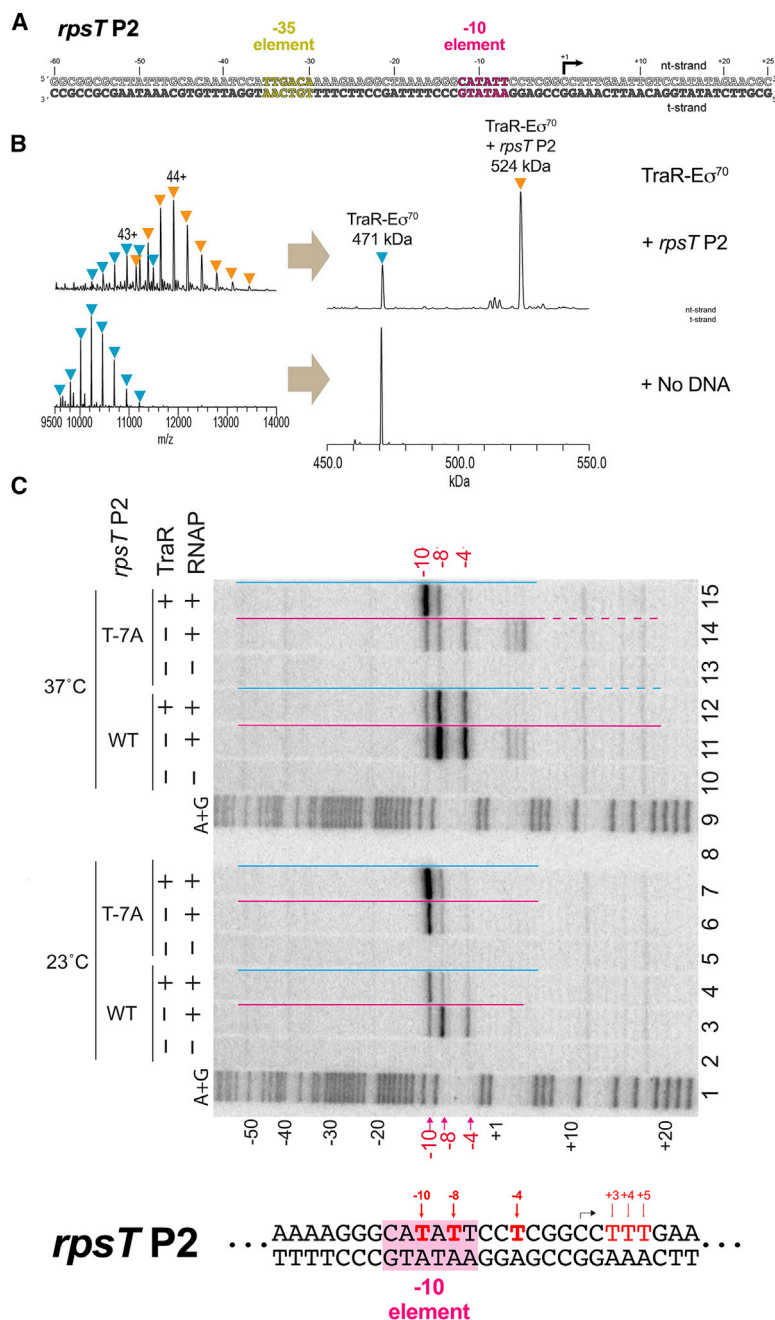


### Figure 1. *Eco* TraR-E $\sigma^{70}$ Forms Stable, Partially Melted Complexes with an *rpsT* P2 Promoter Fragment

(A) The WT-*rpsT* P2 promoter fragment (–60 to +25) used for nMS and cryo-EM.

(B) nMS spectra and the corresponding deconvolved spectra for TraR-E $\sigma^{70}$  complexes with the *rpsT* P2 promoter fragment (A). TraR binds to E $\sigma^{70}$  in a 1:1 stoichiometry, forming a 471-kDa complex. Upon incubation of this complex with the promoter DNA (52 kDa), a predominant charge state series for the TraR-E $\sigma^{70}$ -promoter assembly (524 kDa) was observed.

(C) Detection of unpaired thymines by KMnO<sub>4</sub> footprinting of E $\sigma^{70}$  complexes formed with the WT-*rpsT* P2 or T<sub>–7</sub>A promoters  $\pm$  TraR, and DNase I footprint protection ranges, shown by red or blue lines above each lane (dashed lines: partial protection). Strand cleavage of modified thymines at 23°C (lanes 2–7) or 37°C (lanes 10–15) was detected by gel electrophoresis of DNA fragments <sup>32</sup>P end-labeled in the nt-strand 3' end. Lanes 1 and 9: A+G sequence ladder. Modified thymines at –10, –8 and –4 are indicated in red above and below gel, and on the section of the WT-*rpsT* P2 sequence shown below the gel (–10 element shaded in pink). Black arrow: transcription start site (see Figures S1A and S1B for DNase I footprints at 23°C; for 37°C footprints, see Gopalkrishnan et al., 2017). See also Figure S1.

RPO at most promoters) to +6, with respect to the transcription start site at +1 (Figure 1A) by reduction of the temperature or by the inclusion of TraR. The upstream protection boundary (–54) remained unchanged, indicating that an intermediate complex is formed at *rpsT* P2 either by reducing the temperature or by TraR.

The pattern of unstacked thymines detected by KMnO<sub>4</sub> footprinting (Ross and Gourse, 2009) in these complexes suggested that the transcription bubble was partially melted. At both 23°C and 37°C with RNAP alone, non-template strand (nt-strand) Ts at –10, –8, and –4 were KMnO<sub>4</sub> reactive with RNAP alone (Figure 1C, lanes 3 and 11; Ts at +3, +4, and +5 in the 37°C complex were also reactive; lane 11, indicating “scrunching” of a minor fraction of the complexes at this temperature; Winkelman et al., 2016). The almost-totally conserved nt-strand T at the –7 position (T<sub>–7</sub>(nt); Shultzaberger et al., 2007) was not reactive, reflecting its protection from KMnO<sub>4</sub> by binding in a pocket of  $\sigma^{70}$  subunit domain 2 ( $\sigma^{70}_2$ ) (Feklistov and Darst, 2011).

At 23°C, TraR increased the KMnO<sub>4</sub> signal at –10 and reduced the signals at –8 and –4, suggesting that TraR stabilized a partially melted intermediate (Figure 1C, lane 4). Lower temperature, combined with use of the T<sub>–7</sub>A(nt)-substituted promoter, strengthened the –10 signal even further and eliminated the signal at –4, independent of TraR (Figure 1C, lanes 6 and 7). We infer that all 3 perturbations (TraR, reduced temperature, and T<sub>–7</sub>A(nt)) shift the population to earlier DNA melting intermediates.

The RPO formed on *rpsT* P2 is more stable than on *rmB* P1 but less stable than on many *Eco* promoters (Lemke et al., 2011), and TraR-E $\sigma^{70}$ -*rpsT* P2 complexes were detected by nMS, footprinting (Figures 1, S1A, and S1B), and cryo-EM (Figure 2).

A shift in the occupancy of the *rpsT* P2 promoter from RPO to earlier intermediates was first detected by a shorter length of protected DNAs in DNase I footprints with RNAP at 23°C versus 37°C (Figure 1C, lanes 3 and 11), or upon the addition of TraR at 37°C (Figure 1C, lanes 11 and 12; Gopalkrishnan et al., 2017; protection indicated by colored lines). The downstream protection boundary was shifted from +20 (characteristic of

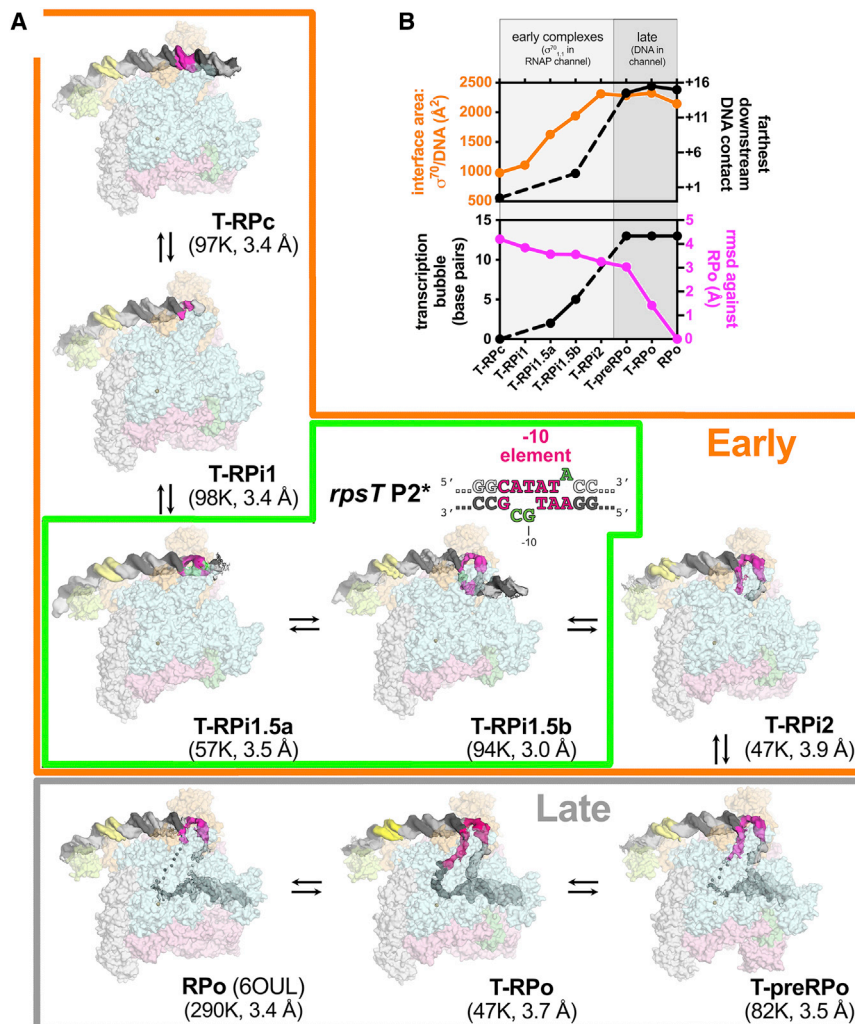


**Figure 2. *Eco*  $E\sigma^{70}$  Promoter Melting Intermediates on the *rpsT* P2 Promoter**

(A) Overall structures of promoter melting intermediates obtained by cryo-EM. Proteins are shown as transparent surfaces ( $\alpha$ ,  $\alpha$ II,  $\omega$ , light gray;  $\alpha$ CTD, pale lemon;  $\beta$ , pale cyan;  $\beta'$ , light pink;  $\sigma^{70}$ , light orange; TraR, pale green). The  $E\sigma^{70}$  active site  $Mg^{2+}$  is shown as a sand-colored sphere. The promoter DNA is shown as cryo-EM difference density (nt-strand, gray; t-strand, dark gray;  $-35$  element, yellow;  $-10$  element, hot pink). The eight structures were derived from three samples. Sample 1: T-RPc, T-RPi1, T-RPi2, T-preRPo, and T-RPo structures were obtained with TraR and the WT-*rpsT* P2 fragment (Figure 1A); sample 2: T-RPi1.5a and T-RPi1.5b were obtained with TraR and *rpsT* P2\* (boxed in green; nucleotide substitutions in *rpsT* P2\* are colored green); and sample 3: RPo was determined previously with WT-*rpsT* P2 without TraR (Chen et al., 2019b). In the early complexes (boxed in green),  $\sigma^{70}_{1,1}$  occupies the  $E\sigma^{70}$  channel. In the late complexes (boxed in gray), downstream duplex DNA occupies the channel.

(B) Structural properties used to order the complexes in the RPo formation pathway. (Top) Plotted in orange (left scale) is the  $\sigma^{70}$ -DNA interface area ( $\text{\AA}^2$ ) (Krissinel and Henrick, 2007). Plotted in black (right scale) is the most downstream protein-duplex DNA contact. For T-RPi1, T-RPi1.5a, and T-RPi2, most or all of the downstream duplex DNA was disordered, so no point is included. (Bottom) Plotted in black (left scale) is the extent of the transcription bubble. For T-RPi1 and T-RPi2, the downstream fork of the transcription bubble was disordered, so no point is included. Plotted in magenta (right scale) is the root-mean-square deviation of  $\alpha$ -carbon positions ( $\text{\AA}$ ) for each complex superimposed with RPo. See also Figures S2–S5 and Table S1.

Two lines of evidence suggest that TraR stabilizes partially open intermediates. First, a higher percentage of *rpsT* P2 DNA was incorporated into complexes with  $E\sigma^{70}$  with TraR than without, as detected by nMS (compare Figures 1B and S1C). Second, the  $KMnO_4$ -reactive band at position  $-10$  seen in the presence of TraR (Figures 1C and S1D, lanes 1 and 2) was also observed when the reaction was performed with RNAP containing a small deletion in the clamp module that prevents stabilizing interactions with downstream duplex DNA in RPo ( $\beta'$   $\Delta$ 215–220-RNAP; Bartlett et al., 1998), but not with promoter DNA alone (Figure S1D, lanes 3–5). These results suggest that rather than populating an earlier intermediate indirectly by destabilizing RPo, TraR stabilizes the earlier intermediate directly (Galburt, 2018; Chen et al., 2019b).

### Structures along the Promoter Melting Pathway

TraR- $E\sigma^{70}$  complexes were incubated with the WT-*rpsT* P2 promoter fragment (Figure 1A) or a promoter variant (*rpsT* P2\*; Figure 2A) engineered to trap early melting intermediates detected by  $KMnO_4$  (Figure 1C, lane 7) and DNase I footprinting (Figure S1A). Noncomplementary base pairs at  $-11$  to  $-10$  were

introduced in *rpsT* P2\* to favor bubble nucleation, while the  $T_{-7A}$ (nt) substitution was made to disfavor propagation of downstream base opening. Basal transcription (without TraR) from *rpsT* P2\* was very weak compared with WT-*rpsT* P2 (Figure S1E), indicating that these substitutions depopulated RPo. TraR inhibited transcription from the WT-*rpsT* P2 promoter fragment (Figure 1A) under conditions similar to those used for cryo-EM (Figure S1F).

The TraR- $E\sigma^{70}$ -promoter complexes were visualized by cryo-EM. Steps of maximum-likelihood classification (Scheres, 2012) revealed 5 TraR- $E\sigma^{70}$ -WT-*rpsT* P2 structures (T-RPc, T-RPi1, T-RPi2, T-preRPo, and T-RPo; Figure 2A) at 3.4–3.9  $\text{\AA}$  nominal resolution and 3.0–3.4  $\text{\AA}$  in the central core of the structures (Figures S2–S4; Table S1). Classification of TraR- $E\sigma^{70}$ -*rpsT* P2\* complexes gave rise to 2 distinct structures (T-RPi1.5a and T-RPi1.5b; Figure 2A) at 3.5 and 3.0  $\text{\AA}$  nominal resolution, respectively (Figures S4 and S5; Table S1). In our structural analysis, we also include a previously determined nominal 3.4- $\text{\AA}$  structure of a complex between  $E\sigma^{70}$  and the WT-*rpsT* P2 promoter fragment prepared in the absence of TraR (RPo; Figure 2A; Chen et al., 2019b).

**A** T-RPc ↔ T-RPi1 ↔ T-RPi1.5a ↔ T-RPi1.5b ↔ T-RPi2 ↔ T-preRPo ↔ T-RPo ↔ RPo

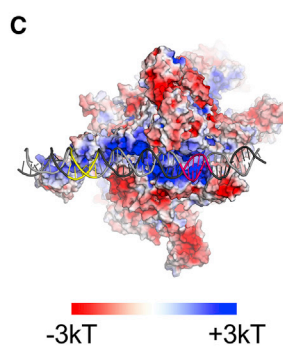
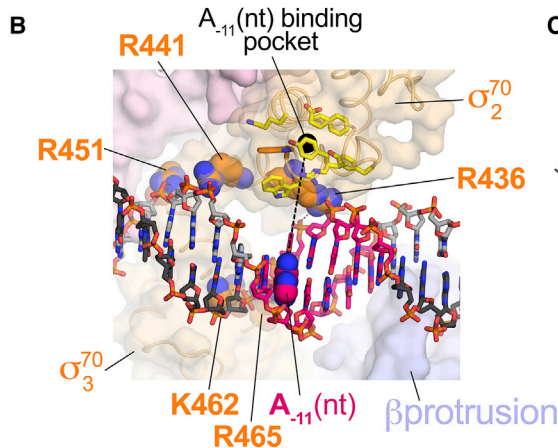
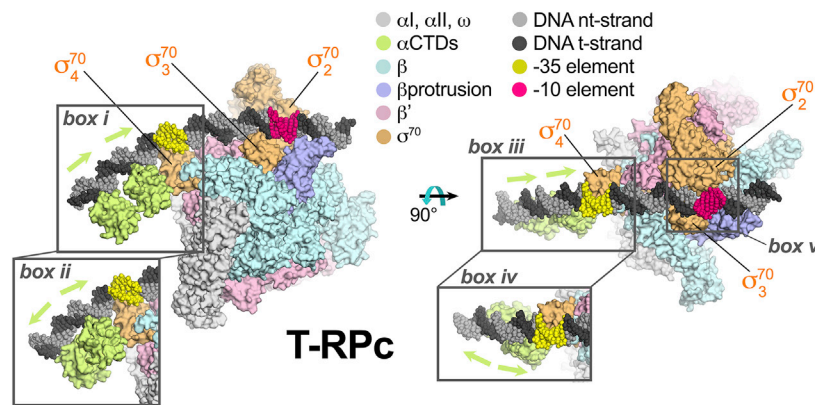


**Figure 3. Structure of the TraR-E $\sigma^{70}$  Closed Promoter Complex (T-RPc)**

The structures determined at top are ordered through the RPo formation pathway (see Figure 2). T-RPc, highlighted in red, is the focus of this figure. (A) Orthogonal views of T-RPc. The proteins are shown as molecular surfaces, DNA is shown as Corey-Pauling-Koltun (CPK) spheres. The proximal (adjacent to  $\sigma^{70}_4$ ) and distal (further upstream)  $\alpha$ CTDs were visualized in two co-existing dispositions on the DNA upstream of the  $-35$  element, head-to-tail (boxes i and iii) and head-to-head (boxes ii and iv). The region around the duplex  $-10$  element (box v) is magnified in (B). (B) Magnified view of E $\sigma^{70}$  interactions with the duplex  $-10$  element showing the absence of sequence-specific interactions (Feklistov and Darst, 2011). The DNA is shown as sticks, with the A $_{-11}$ (nt) base highlighted in CPK spheres, and the location of the cognate binding pocket in  $\sigma^{70}_2$  (yellow side chains) occupied by A $_{-11}$ (nt) in subsequent intermediates indicated by a dashed black line connecting A $_{-11}$ (nt) to the pocket. RNAP is shown as a transparent molecular surface. The side chains shown as CPK spheres ( $\sigma^{70}_2$  R436, R441, R451;  $\sigma^{70}_3$  K462, R465), absolutely conserved among primary  $\sigma$  (Gruber and Bryant, 1997), interact with the duplex DNA phosphate backbone. (C) The electrostatic charge distribution (Baker et al., 2001) is shown on the molecular surface of the T-RPc RNAP (same view as the right view of A). The DNA is shown as an illustration. Color-coding for (A) and (B) is shown in the key. See also Figure S6.

The eight complexes observed by cryo-EM with *rpsT* P2 and *rpsT* P2\* were ordered in the pathway such that the DNA- $\sigma^{70}$  interface area, the downstream boundary of the DNA-RNAP contacts, and the extent of the transcription bubble monotonically increased, while the root-mean-square deviation of  $\alpha$ -carbon positions of each complex compared to RPo decreased monotonically, with progress along the pathway (Figure 2B). A clear demarcation between early and late complexes could be made based on the presence of the N-terminal domain of  $\sigma^{70}$ ,  $\sigma^{70}_{1.1}$  (early complexes), or downstream duplex DNA (late complexes) in the RNAP channel (Bae et al., 2013; Mekler et al., 2002).

In all eight structures, E $\sigma^{70}$  interacts with upstream promoter DNA (from  $-43$  to  $-17$ ) in the same manner: (1) domain 4 of  $\sigma^{70}$  ( $\sigma^{70}_4$ ) engages specifically with the major groove of the promoter  $-35$  element from  $-37$  to  $-30$  (Campbell et al., 2002), (2) an  $\alpha$ -subunit C-terminal domain ( $\alpha$ CTD) binds just upstream of  $\sigma^{70}_4$ , interacting with the DNA minor groove from  $-43$  to  $-38$  (Benoff et al., 2002; Ross et al., 1993, 2001) and with  $\sigma^{70}_4$  (Ross et al., 2003), and (3) conserved residues of the  $\beta'$  zipper ( $\beta'$ Y46 and R47) interact with the DNA backbone from  $-18$  to  $-17$  (Bae et al., 2015; Yuzenkova et al., 2011). By contrast, E $\sigma^{70}$  interacts with the promoter DNA downstream of  $-17$  in diverse configurations that we propose represent steps on the RPo formation pathway (Figure 2A).

**Structure of a Closed Complex**

Initial recognition of the duplex promoter sequence before melting is thought to give rise to the closed complex, RPc (Ruff et al., 2015). RPc has been enriched at some promoters by the formation of the complex at  $0^\circ\text{C}$ – $4^\circ\text{C}$ . DNase I or hydroxyl-radical footprinting revealed an upstream DNA protection in RPc similar to that in RPo (Kovacic, 1987; Schickor et al., 1990). However, downstream protection extended only to  $\sim -3$ , with weak protection sometimes extending to  $\sim +2$  (Kovacic, 1987; Schickor et al., 1990), indicating that the duplex DNA downstream of the  $-10$  element was mostly solvent exposed. The earliest complex in our pathway (T-RPc, Figures 2A and 3), which contains entirely duplex DNA and thus precedes the nucleation of transcription bubble melting, forms E $\sigma^{70}$ -promoter interactions consistent with these earlier footprinting results.

In T-RPc, base-specific protein-DNA interactions do not occur within the  $-10$  element (Figures 3B and S6A), which is consistent with the conclusion that recognition of the  $-10$  element sequence is coupled with melting (Feklistov and Darst, 2011). The duplex  $-10$  element DNA is drawn to a shallow, basic channel on the E $\sigma^{70}$  surface (Figure 3C) by phosphate backbone interactions with invariant basic residues of  $\sigma^{70}_2$  (R436, R441, R451) and  $\sigma^{70}_3$  (K462, R465) (Figure 3B). Sequence-specific recognition of the  $-35$  element by  $\sigma^{70}_4$  fixes the register of the DNA with respect to E $\sigma^{70}$ , positioning the critical and conserved

$A_{-11}(\text{nt})$  (Shultzaberger et al., 2007) in line with the  $\sigma^{70}_2$  residues that ultimately capture the flipped-out base to nucleate transcription bubble formation (Feklistov and Darst, 2011; yellow residues in Figure 3B). DNA downstream of the  $-10$  element ( $-2$  to  $+2$ ) interacts with the tip of the  $\beta$ protrusion, introducing an  $\sim 17^\circ$  bend in the DNA helical axis centered within the  $-10$  element (Figure 3A).

Upstream of the  $\alpha$ CTD proximal to  $\sigma^{70}_4$ , all of the  $E\sigma^{70}\text{-}rpsT\text{P}2$  structures showed cryo-EM density corresponding to a distal  $\alpha$ CTD bound to DNA, but only in T-RPc was this density interpretable. Focused classification of this region upstream of the  $-35$  element revealed two dispositions of the  $\alpha$ CTDs, head-to-head ( $\sim 53\%$  of the particles) and head-to-tail ( $\sim 47\%$ ), with altered upstream DNA trajectory (Figure 3A, compare boxes iii and iv). In all of the cases, the linkers connecting the  $\alpha$ CTDs with the  $\alpha$ NTDs were disordered, therefore we could not assign which  $\alpha$ NTD was connected to which  $\alpha$ CTD. These structures highlight the dynamic nature of the flexibly tethered  $\alpha$ CTDs, which tune expression via variable interactions with  $\sigma^{70}_4$ , transcription factors, and upstream DNA sites (Ross et al., 1993, 2003; Estrem et al., 1998; Ross and Gourse, 2005; Benoff et al., 2002; Lee et al., 2012).

### Transcription Bubble Nucleation and the $\sigma^{70}$ W-Dyad

The key event in the nucleation of promoter melting is thought to be the flipping of the  $A_{-11}(\text{nt})$  base from the duplex DNA into its  $\sigma^{70}_2$  pocket (Chen and Helmann, 1997; Feklistov and Darst, 2011; Heyduk et al., 2006; Lim et al., 2001) and isomerization of an invariant W-dyad of  $\sigma^{70}_2$  (W433/W434) from an “edge-on” (Figures 4B and 4C) to a “chair”-like conformation (Figure 4D). In the chair conformation, the W433 side chain rotates away from W434, fills the space vacated by the flipped-out  $A_{-11}(\text{nt})$ , and forms a  $\pi$ -stack with the face of the exposed  $-12(\text{nt})$  base (Bae et al., 2015).

In T-RPi1, the  $A_{-11}(\text{nt})$  base is flipped and entering its cognate  $\sigma^{70}_2$  pocket (Figure 4C). Notably, the W-dyad remains in its edge-on conformation (Figure S6B). The edge-on orientation of the W433 side chain in T-RPi1 sterically clashes with the  $-12$  bp, and the cryo-EM density indicates transient melting of the  $-12$  bp in this intermediate (Figures 4C and S6B). In all of the subsequent structures in the pathway (T-RPi1.5a  $\rightarrow$  RPo), the flipped-out  $A_{-11}(\text{nt})$  base is fully engaged in its pocket and the  $-12$  nucleotides are clearly base paired (Figures 4D and S6C). In T-RPi1.5b  $\rightarrow$  RPo, W433 is rotated into the chair conformation and stacked with the  $-12(\text{nt})$  base, but in the T-RPi1.5a intermediate (between T-RPi1 and T-RPi1.5b), the cryo-EM density for W433 is poorly resolved and does not unambiguously define the edge-on or chair conformations (Figure S6C). We modeled T-RPi1.5a with W433 in the chair conformation due to the strong apparent density for the  $-12$  bp, but we propose that in T-RPi1.5a, the conformation of W433 and the disposition of the  $-12$  bp is dynamic, giving rise to the poorly resolved cryo-EM density.

Although there is fragmented cryo-EM density for the downstream duplex DNA in T-RPi1, the density is uninterpretable, and we have not modeled the downstream edge of the transcription bubble or the downstream DNA (Figure 4C). Nevertheless, T-RPi1 supports a model in which transcription bubble nucle-

ation begins before DNA enters the RNAP cleft. The entire T-RPc  $\leftrightarrow$  T-RPi1  $\leftrightarrow$  T-RPi1.5a transition, illustrating transcription bubble nucleation and possible W-dyad isomerization, is shown in Video S1.

### Transcription Bubble Propagation and the Protrusion Pocket

In T-RPi1.5a (obtained with *rpsT* P2\*; Figure 2A), the nascent transcription bubble is only 2 nt (the engineered bubble from  $-11$  to  $-10$ ), and density for  $\sim 7$  bp of downstream duplex DNA is interpretable (Figure 4D). Further along the pathway, in the transition from T-RPi1.5a to T-RPi1.5b, the transcription bubble extends to 5 nt ( $-11$  to  $-7$ ), the flipped-out  $A_{-11}(\text{nt})$  completely engages its cognate  $\sigma^{70}_2$  pocket, and nt-strand phosphate-backbone interactions from  $-10$  to  $-8$  with  $\sigma^{70}_2$  are established as in RPo (Figures 5A–5C). Presumably because of the  $T_{-7}A(\text{nt})$  substitution in *rpsT* P2\* (Figure 5A), the mutant  $A_{-7}(\text{nt})$  base is not engaged in the  $\sigma^{70}_2$  pocket normally occupied by the conserved  $T_{-7}(\text{nt})$ , and the entire  $-7(\text{nt})$  nucleotide is disordered (Figure 5C).

In all of the structures with TraR bound (except for T-RPo), TraR establishes a significant interface with the RNAP  $\beta$ lobe-Si1 domains, inducing an  $\sim 18^\circ$  rotation of the  $\beta$ lobe-Si1 toward TraR and away from the  $\beta$ protrusion (Figures 5B and 5C) (Chen et al., 2019b). Rotation of the  $\beta$ lobe-Si1 widens the gap between the  $\beta$ protrusion and the  $\beta$ lobe by  $\sim 9$  Å (Figure S5D). The new position of the  $\beta$ lobe alters  $\beta$ lobe- $\sigma^{70}_{1,1}$  interactions (Chen et al., 2019b), but interactions between the  $\beta$ lobe-gate-loop (GL;  $\beta$  residues 371–376) and  $\sigma^{70}_{1,1}$  that pinch off further DNA access to the RNAP cleft are maintained. The GL barrier hinders further DNA melting and entry into the RNAP cleft, while the widened gap between the  $\beta$ protrusion and  $\beta$ lobe provides a channel to accommodate the downstream duplex DNA (Figure 5C). The T-RPi1.5a  $\leftrightarrow$  T-RPi1.5b transition is shown in Video S2.

Because of the short transcription bubble and the novel disposition of the downstream duplex DNA, the single-stranded t-strand DNA in TraR1.5b follows a path between  $\sigma^{70}_2$  and the  $\beta$ protrusion that is not as deep into the RNAP cleft as complexes later in the pathway (Figure 5D). In this intermediate path of the DNA, the  $-9$  t-strand base ( $T_{-9}(\text{t})$ ) flips toward the  $\beta$ protrusion and binds in a distinct pocket in the underside of the  $\beta$ protrusion that has not been described previously (referred to here as the protrusion pocket; Figures 5D and S7A). The  $T_{-9}(\text{t})$  is protected from  $\text{KMnO}_4$  reactivity in the presence of TraR compared to without TraR (Figure S7B), presumably due to protrusion pocket binding. Residues that form the protrusion pocket and interact with  $T_{-9}(\text{t})$  (Figure 5D) are conserved among bacterial RNAPs, especially in proteobacteria such as *Eco* (Figure S7C), pointing to functional importance. The backbone carbonyl of  $\beta$ M492 and the backbone amide of  $\beta$ N494 form hydrogen bonds with the  $T_{-9}(\text{t})$  base, suggesting that the protrusion pocket is thymine specific (Figures 5D and S7A). The protrusion pocket would be unable to accommodate a purine without significant rearrangement of the DNA phosphate backbone (Figure S7D).

To test whether binding of  $T_{-9}(\text{t})$  in the protrusion pocket has functional consequences, we constructed structure-guided RNAP protrusion pocket mutants  $\beta$ A474V and  $\beta$ A474L. These substitutions were expected to fill the pocket, excluding the

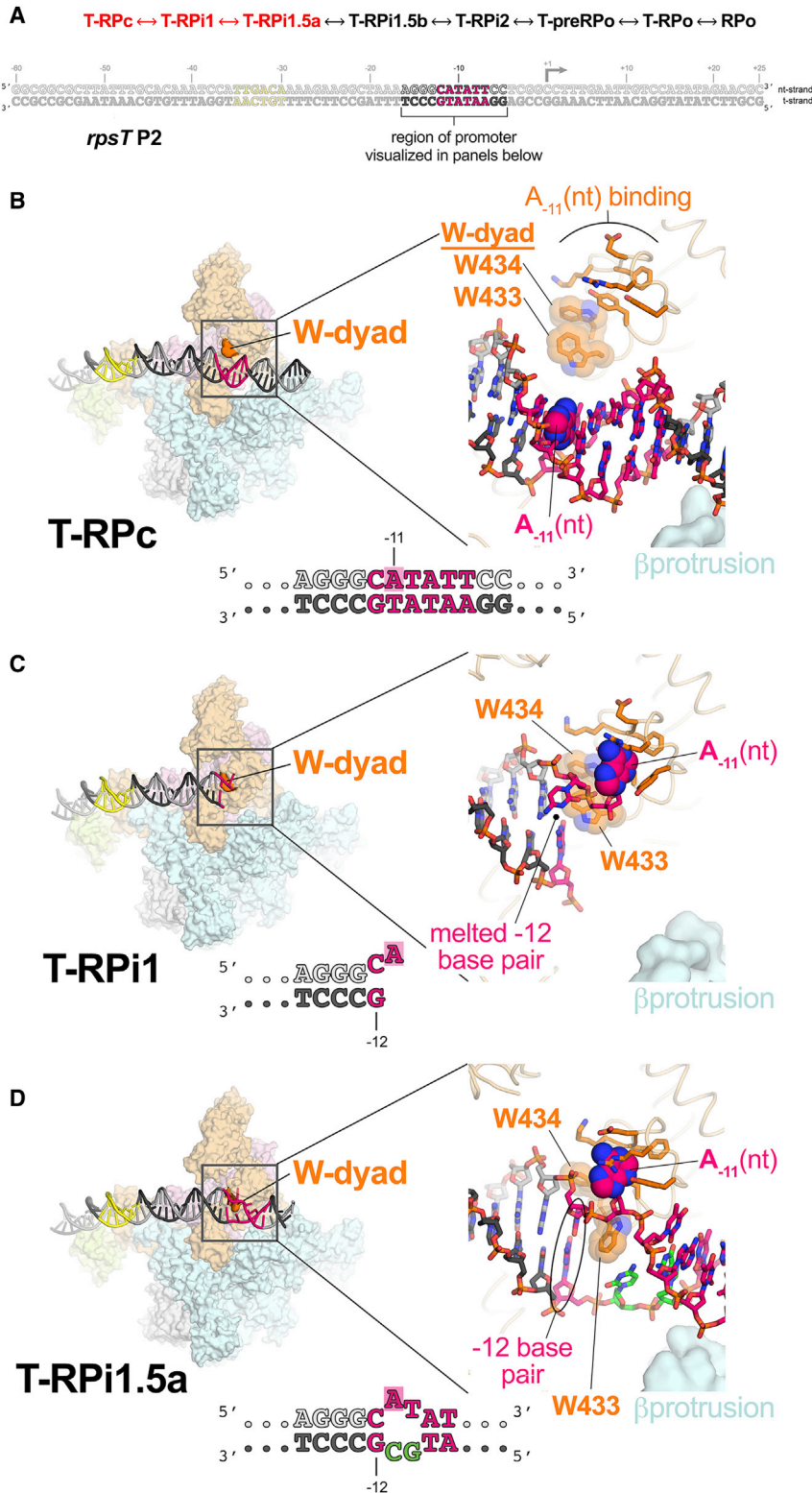


**Figure 4. T-RPc ↔ T-RPi1 ↔ T-RPi1.5a; Transcription Bubble Nucleation**

(A) At top, the order of structures through the RPO formation pathway (see Figure 2). The progression from T-RPc ↔ T-RPi1 ↔ T-RPi1.5a, highlighted in red, is the focus of this figure. (Bottom) The sequence of the duplex *rpsT* P2 promoter fragment is shown, with the region of the promoter visualized in the panels below highlighted.

(B–D) At left, overall view of T-RPc (B), T-RPi1 (C), and T-RPi1.5a (D).  $\sigma^{70}$  is shown as a molecular surface with promoter DNA shown as an illustration (color-coded as in Figure 2A). The  $\sigma^{70}$  W-dyad is dark orange. The boxed region is magnified at right. (Right) Magnified view of promoter –10 element and W-dyad. Promoter DNA is shown in stick format with the A<sub>-11</sub>(nt) base highlighted with CPK spheres.  $\sigma^{70}$  is shown as a backbone worm (pale orange), but with side chains of residues that interact with A<sub>-11</sub>(nt) in RPO shown (orange). The W-dyad is highlighted with transparent CPK spheres.

(B) T-RPc: The –10 element is completely duplex and the W-dyad is in the edge-on conformation.

(C) T-RPi1 and transcription bubble nucleation: A<sub>-11</sub>(nt) is flipped out of the duplex toward its cognate  $\sigma^{70}_2$  pocket, nucleating –10 element melting. Steric clash with the edge-on conformation of the W-dyad disrupts the –12 bp. Downstream DNA lacks cryo-EM density and is presumed to be highly dynamic.

(D) T-RPi1.5a: the flipped-out A<sub>-11</sub>(nt) more fully engages with its cognate  $\sigma^{70}_2$  pocket. We modeled the W-dyad in its chair conformation (Bae et al., 2015), allowing the –12 bp to reform. The T-RPi1.5a structure was obtained with the mutant *rpsT* P2\* promoter (base substitutions are green). See also Figure S6 and Video S1.

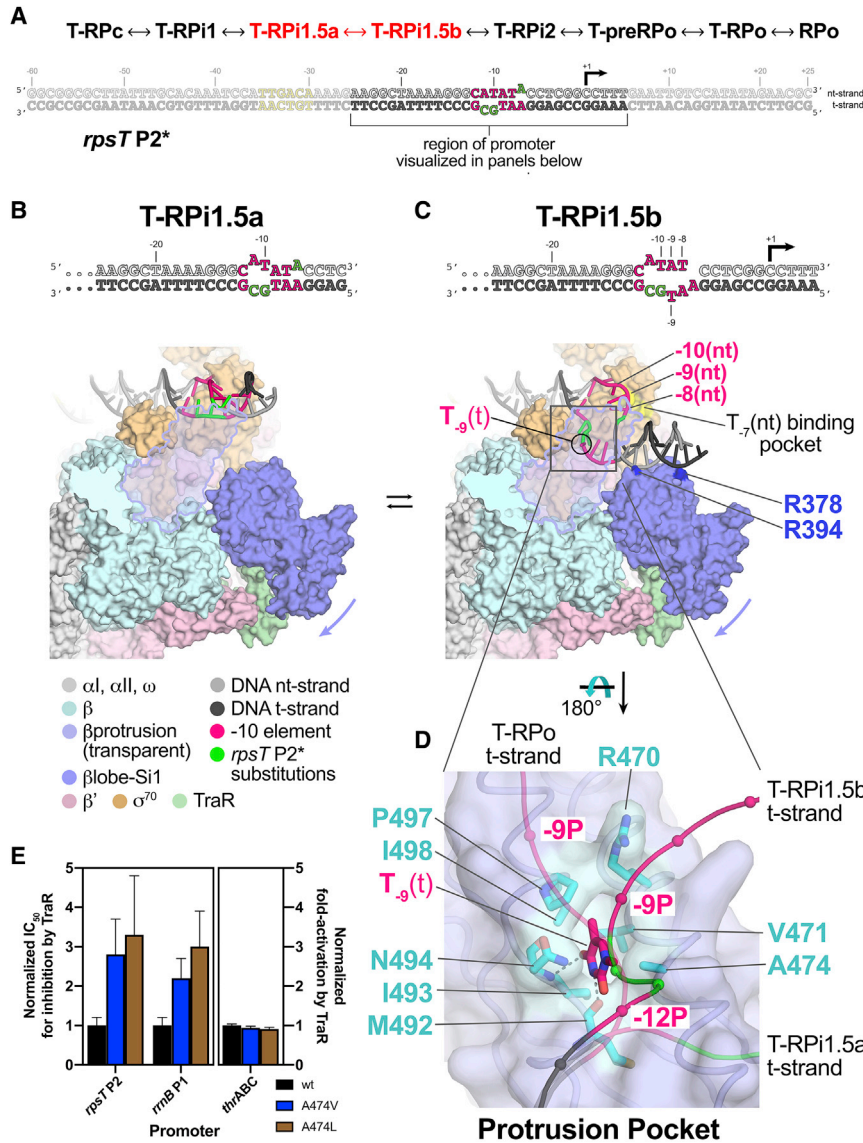


**Figure 5. T-RPi1.5a ↔ T-RPi1.5b; Transcription Bubble Propagation and the Protrusion Pocket**

(A) At top, the order of structures through the RPo formation pathway (see Figure 2). The progression from T-RPi1.5a ↔ T-RPi1.5b, highlighted in red, is the focus of this figure. (Bottom) The sequence of *rpsT* P2\* is shown, with the region of the promoter visualized in the panels below highlighted.

(B and C) Overall view of T-RPi1.5a (B) and T-RPi1.5b (C).  $E\sigma^{70}$  is illustrated as a molecular surface with promoter DNA (color-coded as in the key). The  $\beta$ protrusion (light blue) is transparent, with an outline. The rotation of the  $\beta$ lobe-Si1 domains (slate blue) induced by TraR is indicated by the slate blue arrow.

(B) T-RPi1.5a.

(C) In T-RPi1.5b, DNA phosphate backbone contacts between nt-strand -10 to -8 and  $\sigma^{70}$  are established as in RPo. The -7(nt) base is positioned over its cognate pocket in  $\sigma^{70}$  (highlighted in yellow), but is not bound in the pocket due to the T<sub>-7</sub>A(nt) substitution of *rpsT* P2\*. The T<sub>-9</sub>(t) base flips up and is bound in the protrusion pocket on the underside of the  $\beta$ protrusion.  $\beta$ lobe residues R378 and R394, 2 of many residues that interact with the DNA in T-RPi1.5b, but not in RPo (Table S2), are highlighted (dark blue).

(D) The protrusion pocket, viewed from the underside of the  $\beta$ protrusion. The  $\beta$ protrusion is shown as a backbone worm with a transparent molecular surface. The T-RPi1.5b t-strand DNA is shown as a thin backbone worm with phosphate atom positions denoted by CPK spheres. The T<sub>-9</sub>(t) base, bound in the protrusion pocket, is shown as sticks. The t-strand DNA backbone paths for T-RPi1.5a (precedes T-RPi1.5b in the RPo formation pathway) and T-RPo (follows T-RPi1.5b) are shown for comparison. Protrusion pocket residues that interact with the T<sub>-9</sub>(t) base are shown as sticks and colored cyan. Thymine-specific hydrogen bonds between RNAP and T<sub>-9</sub>(t) are denoted by dark gray dashed lines.

(E) Effect of  $\beta$ A474 substitutions on TraR-mediated inhibition of *rpsT* P2 and *rmbP1* promoters (left) or activation of *thrABC* (right). For *rpsT* P2 and *rmbP1*, IC<sub>50</sub> values for TraR inhibition of WT-RNAP

(black bar),  $\beta$ A474V-RNAP (blue bar), and  $\beta$ A474L-RNAP (brown bar) are plotted relative to WT-RNAP (normalized to 1.0). For *thrABC*, fold-activation (relative to no TraR) at 500 nM TraR is plotted relative to WT-RNAP (normalized to 1.0). Averages with SDs from 3 independent experiments are shown.

See also Figures S6 and S7, Table S2, and Video S2.

thymine base (Figure 5D). There was a significant increase (2- to 3-fold) in the half-maximal inhibitory concentration (IC<sub>50</sub>) for the inhibition by TraR of 2 promoters containing T<sub>-9</sub>(t), WT-*rpsT* P2 and *rmbP1*, with the greater effect resulting from the substitution with the larger side chain (Figures 5E, S7E, and S7F). Thus, steric occlusion of the pocket by these RNAP substitutions reduces the efficiency of TraR inhibition. We conclude that T<sub>-9</sub>(t) binding in the protrusion pocket contributes to TraR-mediated stabilization of intermediate T-RPi1.5b, and that this stabilization is important for the mechanism of inhibition by TraR. By contrast, the protrusion pocket substitutions had no effect on the activation of *thrABC* by TraR, as expected (Figures 5E and S7G), since this promoter has a t-strand G at -9 (G<sub>-9</sub>(t)) instead of a T, and this

step is not rate limiting at activated promoters (Chen et al., 2019b). The RNAP substitutions did not affect basal transcription at the limited number of promoters tested here. We suggest that eliminating the T<sub>-9</sub>(t) interaction in the protrusion pocket would affect only promoters with the appropriate kinetic characteristics (Galburt, 2018; Chen et al., 2019b).

In T-RPi1.5b, promoter DNA establishes many  $E\sigma^{70}$  contacts that are unique to this intermediate; these contacts are either altered or absent in the subsequent RPo-like complexes (T-RPo or RPo; Table S2). Like the conserved residues that form the protrusion pocket interaction with T<sub>-9</sub>(t) in T-RPi1.5b (Figure 5D), many other conserved residues in the  $\beta$ protrusion,  $\beta$ lobe, and  $\sigma^{70}$  participate in promoter contacts in T-RPi1.5b,

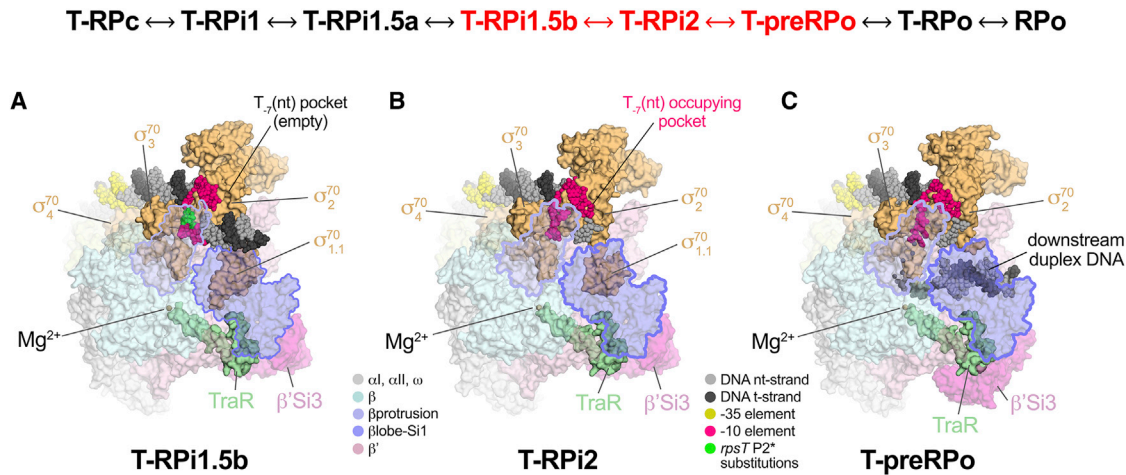


**Figure 6. T-RPi1.5b ↔ T-RPi2 ↔ T-preRPO; Transcription Bubble Completion and  $\sigma^{70}_{1,1}$  Ejection**

At top, the order of structures through the RPo formation pathway (see Figure 2). The progression from T-RPi1.5b ↔ T-RPi2 ↔ T-preRPO, highlighted in red, is the focus of this figure.

(A–C) Overall view of T-RPi1.5b (A), T-RPi2 (B), and T-preRPO (C).  $E\sigma^{70}$  is shown as molecular surfaces, with core RNAP transparent, revealing the RNAP active site  $Mg^{2+}$  (sand-colored sphere), TraR in the secondary channel, and either  $\sigma^{70}_{1,1}$  (T-RPi1.5b and T-RPi2) or downstream duplex DNA (T-preRPO) in the RNAP channel. The  $\beta$ protrusion (light blue, transparent) and  $\beta$ lobe-Si1 (slate blue, transparent) are outlined.

(A) T-RPi1.5b: downstream duplex DNA is accommodated in the gap between the  $\beta$ protrusion and  $\beta$ lobe-Si1. The empty  $T_{-7}(nt)$  pocket in  $\sigma^{70}_2$  is denoted.

(B) T-RPi2: the  $-10$  element  $T_{-7}(nt)$  is engaged in its cognate  $\sigma^{70}$  pocket, the transcription bubble advances in the downstream direction, and the single-stranded nt-strand downstream to  $-4$  is positioned in the complex, much like RPo. The downstream edge of the transcription bubble and downstream duplex DNA are disordered and  $\sigma^{70}_{1,1}$  occupies that RNAP channel.

(C) T-preRPO: the transcription bubble is fully formed ( $-11$  to  $+2$ ). The downstream duplex DNA is accommodated in the RNAP channel in place of the ejected  $\sigma^{70}_{1,1}$ .

See also Videos S3 and S4.

but not in later complexes (Table S2). Substitution of these residues would be expected to affect RPo formation by altering the multi-step energy landscape of RPo formation, even though they do not interact with promoter DNA in RPo itself. RNAPs with substitutions for  $\beta R378$  and  $\beta R394$ , basic residues that interact with promoter DNA in T-RPi1.5b but not in RPo (Figure 5C), were defective not only in TraR-mediated inhibition but also in basal transcription (Figure S7H), which is consistent with a model in which  $E\sigma^{70}$ -promoter interactions that stabilize the T-RPi1.5b intermediate are important for TraR-mediated inhibition and for transcription in the absence of TraR.

### $\sigma^{70}_{1,1}$ Ejection

In T-RPi2, the intermediate following T-RPi1.5b,  $T_{-7}(nt)$  is engaged in its  $\sigma^{70}_2$  pocket, and the single-stranded nt-strand DNA from  $-11$  to  $-5$  interacts with the RNAP in a manner similar to that in RPo, but in contrast to RPo,  $\sigma^{70}_{1,1}$  remains in the RNAP cleft (Figures 6A and 6B). The 5-nt transcription bubble of T-RPi1.5b is extended to at least 6 nt, but the full extent of the T-RPi2 transcription bubble cannot be determined because the downstream single-stranded-double-stranded(ss-ds) junction and the downstream duplex DNA in this complex lack cryo-EM density (Figure 6B). Masking, particle subtraction, and focused classification approaches failed to identify interpretable density for the downstream DNA, indicating that it is highly dynamic.

In the next intermediate (T-preRPO), the transcription bubble is fully formed (13 nt, from  $-11$  to  $+2$ ) and the downstream duplex DNA occupies the RNAP channel, displacing  $\sigma^{70}_{1,1}$  (Figure 6C)

and initiating the late stages of the pathway (Figure 2). We call this complex T-preRPO because the  $\beta$ lobe-Si1 is still in its rotated conformation, interacting with TraR, which remains bound to the complex (Figures 6C and S7I).

Next in the pathway is T-RPo, in which TraR remains bound, but the rest of the RNAP, including the  $\beta$ lobe-Si1, attains an RPo-like conformation (Figure S7I). Although the DNA is in an RPo-like state, T-preRPO and T-RPo would not be transcriptionally active because the presence of TraR sterically blocks folding of the trigger-loop (critical for efficient catalysis) (Vassilyev et al., 2007; Wang et al., 2006; Windgassen et al., 2014) and also blocks binding of the 3'-NTP substrate (Chen et al., 2019b).

## DISCUSSION

We observed seven different intermediate structures that delineate changes in the conformation of both  $E\sigma^{70}$  and the *rpsT* P2 promoter on the pathway to forming transcription-capable RPo. These intermediates were observed in the presence of TraR, which inhibits transcription from *rpsT* P2 by increasing the occupancy of intermediates earlier in the kinetic pathway (Rutherford et al., 2009; Gopalkrishnan et al., 2017), facilitating their structure determination.

Analysis of the structures of RPo intermediates provides insights into the mechanism of transcription initiation. Early intermediates reveal unanticipated transient events, including the melting of the  $-12$  bp and capture of the  $T_{-9}(t)$  base. We propose that these intermediate structures define steps in DNA opening

at most if not all  $E\sigma^{70}$  promoters and discuss the implications of this model for regulation. Finally, we outline how these complexes inform models of DNA opening.

### The RNAP Clamp

Clamp dynamics play an important role in promoter melting for all cellular RNAPs (Boyaci et al., 2019; Chakraborty et al., 2012; Feklistov et al., 2017; He et al., 2013; Schulz et al., 2016). In our cryo-EM structures of TraR bound to  $E\sigma^{70}$ , the range of clamp motions in solution was narrowed by TraR binding (Chen et al., 2019b). Analysis of RNAP clamp positions in the TraR- $E\sigma^{70}$ -promoter intermediates (relative to RPo) revealed that the initial  $E\sigma^{70}$ -promoter complex, T-RPc, has the most open clamp (7.2° open; Figure S7I). Transient closing of the clamp in T-RPc would pinch the DNA between the  $\beta$ protrusion and  $\sigma^{70}_2$  (Figure 3A), which may respond by untwisting, facilitating  $A_{-11}(\text{nt})$  flipping and capture by  $\sigma^{70}_2$ , thereby initiating bubble nucleation (Feklistov et al., 2017). In the early intermediate complexes in which  $A_{-11}$  capture is first detected (T-RPi1–T-RPi1.5b), the clamp is ~5° open. The clamp generally closes as the pathway approaches RPo, but not monotonically (Figure S7I).

### RPo Formation Involves Transient Melting of the –12 bp

The first intermediate visualizing bubble nucleation, T-RPi1, reveals that  $A_{-11}(\text{nt})$  capture occurs before or concurrent with W-dyad isomerization and results in transient –12 bp melting due to steric clash with W433 (Figures 4C and S6B). Subsequently, the W433 side chain rotates into the chair conformation, relieving steric clash and stabilizing –12 bp formation by stacking on the exposed downstream face of the –12(nt) base (Figures 4D and S6C). We suggest that this transient –12 bp melting may occur at most promoters and could help explain the conservation of the TA bp at the –12 position (Shultzaberger et al., 2007).

### T-RPi1.5b Is Likely on the Pathway during Basal RPo Formation and Is Stabilized by TraR

We designed *rpsT* P2\* to trap an early melting intermediate detected by footprints of complexes formed on a fully duplex *rpsT* P2  $T_{-7}A$  promoter fragment. Protection of this intermediate against DNase I extends downstream to ~+6 (Figure S1A), and the transcription bubble likely extends from –11 to between –8 and –5, corresponding to a bubble of 4–8 nt (Figure 1C, lanes 6 and 7). T-RPi1.5b, the prominent intermediate observed by cryo-EM with *rpsT* P2\* (Figures 2A, 5C, and 6A), has a transcription bubble of 5 nt (–11 to –7) and downstream DNA contacts that extend to +4. Since the size of the transcription bubble detected by  $\text{KMnO}_4$  footprinting and the limits of DNase I protection of the *rpsT* P2  $T_{-7}A$  promoter are consistent with the properties of the T-RPi1.5b complex, we conclude that the structurally and biochemically detected intermediate are the same, indicating that the pre-formed bubble in *rpsT* P2\* is not required for the formation of the intermediate.

Several lines of evidence support the hypothesis that the T-RPi1.5b intermediate, or a similar complex, is on the normal RPo formation pathway, even in the absence of TraR. First, at 23°C, the  $\text{KMnO}_4$  and DNase I footprints on the *rpsT* P2( $T_{-7}A$ ) promoter were very similar with or without TraR (Figure 1C, lanes

6 and 7), indicating that TraR is not required for its formation. Second, substitutions of  $E\sigma^{70}$  residues that interact with the DNA in T-RPi1.5b but not in RPo affect “basal” transcription (i.e., transcription in the absence of TraR) and inhibition by TraR (Figure S7H). Third, the *rpsT* P2\* promoter fragment contains mismatched base pairs within the –10 element (Figure 2A), and thus would be expected to stimulate basal transcription compared to the duplex WT-*rpsT* P2 promoter. However, transcription from *rpsT* P2\* in the absence of TraR is weaker than transcription from WT-*rpsT* P2 (35% of WT-*rpsT* P2; Figure S1E), suggesting that pre-melting upstream bases does not provide enough free energy to overcome subsequent conversions when the conserved  $T_{-7}(\text{nt})$  is replaced by adenine. This demonstrates the key role of  $T_{-7}(\text{nt})$  binding to its cognate  $\sigma^{70}$  pocket (Feklistov and Darst, 2011) in driving subsequent opening (see below).

### T-RPi2, $\sigma^{70}_{1,1}$ Ejection, and Completion of the Transcription Bubble

The finding that *rpsT* P2\* (with the  $T_{-7}A(\text{nt})$  substitution) yields the stable intermediate T-RPi1.5b with  $\sigma^{70}_{1,1}$  occupying the RNAP channel without proceeding to RPo, while the WT-*rpsT* P2 yields RPo-like complexes in which the downstream duplex DNA displaces  $\sigma^{70}_{1,1}$  (despite the presence of TraR), suggests that engagement of  $T_{-7}(\text{nt})$  with its cognate  $\sigma^{70}_2$  pocket is an important determinant of  $\sigma^{70}_{1,1}$  ejection. The pathway progresses from T-RPi1.5b, with its 5-nt transcription bubble, to T-preRPo with its complete 13-nt transcription bubble through a single intermediate (T-RPi2) in which the extent of the transcription bubble and the path of the downstream duplex DNA are highly dynamic (Figure 6). This suggests that propagation of the transcription bubble downstream to the start site (from ~–4 to +2) occurs rapidly following nucleation and melting of the –10 element, which is consistent with kinetic analyses of RPo formation (Hubin et al., 2017a; Ruff et al., 2015; Saecker et al., 2011).

### The Complete RPo Formation Pathway and TraR Binding

Video S3 illustrates the entire RPo formation pathway, starting with the  $\beta$ lobe-Si1 rotation induced by TraR binding to RNAP. The  $\beta$ lobe-Si1 remains rotated throughout most of the pathway (until T-RPo), reflecting TraR binding, but how does this relate to basal RPo formation in the absence of TraR? Only one intermediate on the pathway, T-RPi1.5b, appears to require  $\beta$ lobe-Si1 rotation for its formation. We argue above that T-RPi1.5b is on the basal pathway, and by extension, we suggest that  $\beta$ lobe-Si1 rotation occurs at this point during the basal pathway, but transiently. In early steps of the pathway preceding T-RPi1.5b (T-RPc  $\leftrightarrow$  T-RPi1  $\leftrightarrow$  T-RPi1.5a), the promoter DNA is far from the  $\beta$ lobe-Si1 and it does not appear that  $\beta$ lobe-Si1 rotation would affect these steps directly, suggesting that the salient structural features of these intermediates (binding of duplex DNA in T-RPc, transcription bubble nucleation in T-RPi1, and subsequent W-dyad isomerization) reflect steps in the standard RPo formation pathway with or without TraR. TraR stabilization of the  $\beta$ lobe-Si1 rotation likely increases the occupancy of these early intermediates by increasing the population of T-RPi1.5b, facilitating our analysis of their structure.

Video S4 illustrates the hypothetical RPo formation pathway in the absence of TraR.

### Five Base-Specific Pockets in $E\sigma^{70}$ Modulate RPo Formation

We note that RPo formation is controlled, in part, by base-specific pockets distributed throughout the  $E\sigma^{70}$  structure. The cognate pockets for  $A_{-11}(\text{nt})$  and  $T_{-7}(\text{nt})$  in  $\sigma^{70}$  are essential for transcription bubble nucleation and  $-10$  element melting (Feklistov and Darst, 2011), and these interactions are maintained in the final RPo. The protrusion pocket discovered here binds  $T_{-9}(\text{t})$  transiently (Figure 5D), contributing to regulation by TraR (Figure 5E), and may play a role in RPo formation in the absence of factors (Figure 1C, lane 6). A binding site for  $G_{-5}(\text{nt})$  also plays a role in modulating RPo lifetime and regulation by ppGpp/DksA (Haugen et al., 2006; 2008b). Finally,  $G_{+2}(\text{nt})$  binds in an RNAP  $\beta$ -subunit pocket (Zhang et al., 2012). These 5 separate pockets and the myriad possible interactions with different promoter sequences give rise to a combinatorial effect that contributes to the 10,000-fold variation in initiation rates *in vivo* and *in vitro* (McClure, 1985; Ruff et al., 2015).

While  $A_{-11}(\text{nt})$  and  $T_{-7}(\text{nt})$  are present in nearly all  $E\sigma^{70}$  promoters (Shultzaberger et al., 2007; Feklistov and Darst, 2011),  $G_{-5}(\text{nt})$  and  $G_{+2}(\text{nt})$  are not conserved but modulate RPo formation when they are present (Haugen et al., 2006; Zhang et al., 2012).  $T_{-9}(\text{t})$  is also not strongly conserved, but it is enriched in promoters that are negatively regulated, and underrepresented in promoters that are positively regulated, by DksA/ppGpp and TraR (Sanchez-Vazquez et al., 2019). This illustrates how transcription factor promoter specificity can depend on DNA sequences that contribute to the occupancy of transient intermediates that are not represented in the initial or final steps in the mechanism.

### Relation to Previously Identified Intermediates

It has long been appreciated that RPo formation is a multi-step process (Buc and McClure, 1985; Hawley and McClure, 1982; Kadesch et al., 1982; Roe et al., 1984; Rosenberg et al., 1982; Walter et al., 1967). RPo formation intermediates of *Eco*  $E\sigma^{70}$  have been characterized on several promoters (Rogozina et al., 2009; Rutherford et al., 2009; Sclavi et al., 2005), none more extensively than  $\lambda P_R$ , where 3 “kinetically significant” intermediates in RPo formation at  $\lambda P_R$ ,  $I_1$ ,  $I_2$ , and  $I_3$  have been identified (reviewed in Ruff et al., 2015).  $I_1$  is proposed to comprise an ensemble of closed complexes. The rate-limiting conversion from  $I_1$  to  $I_2$  involves opening the entire transcription bubble, loading the DNA into the RNAP cleft, and ejecting  $\sigma^{70}_{1,1}$  (Ruff et al., 2015). Thus, partially melted intermediates have not been observed at this promoter.

A study of the kinetics of RPo formation by *Mycobacterium tuberculosis* (*Mtb*) RNAP on the *Mtb* *rrnA* P3 promoter identified a minimum of 2 significant intermediates, termed RP1 and RP2 (Hubin et al., 2017a). The structure of a partially melted intermediate, proposed to correspond to RP2, was revealed by cryo-EM (Boyaci et al., 2019). The intermediate contained an 8-nt bubble ( $-11$  to  $-4$ ). The RP2 intermediate is not structurally similar to any of the intermediates observed here, but it would lie between T-RPi2 and T-preRPo. Given the differences in the nature of the N-terminal domains of *Mtb*  $\sigma^A$  and *Eco*  $E\sigma^{70}$  (Hubin

et al., 2017b), in lineage-specific insertions in  $\beta$  and  $\beta'$  (Lane and Darst, 2010), and the presence of *Mtb* factors not found in *Eco* (Hubin et al., 2017a), it is unclear whether *Eco*  $E\sigma^{70}$  would significantly populate an equivalent intermediate. Thus, it is not surprising that an RP2-like complex was not observed here with *Eco*  $E\sigma^{70}$ .

Clearly, the two or three significant intermediates identified at *Mtb* *rrnA* P3 and *Eco*  $\lambda P_R$  cannot account for the seven intermediates observed here (Figure 2A). We suggest that ensemble footprinting or fluorescence approaches do not have the sensitivity and/or temporal resolution to distinguish some of the intermediates identified in our structures. Thus,  $I_1$ ,  $I_2$ ,  $I_3$ , RP1, RP2, and other intermediates described previously are likely ensembles of many intermediates that accumulate at kinetic bottlenecks along the RPo formation pathway.

Does DNA opening involve the same steps at every promoter or does the pathway depend on promoter sequence? We propose that RPo formation by  $E\sigma^{70}$  proceeds through very similar conformational changes defined by these intermediates, whether or not assisted by transcription factors. Because binding free energy drives each interconversion, the overall net gain in  $E\sigma^{70}$ -DNA interactions versus the cost of duplex DNA disruption at each step determines the corresponding rate constants (Haugen et al., 2008a; Ruff et al., 2015). As DNA sequence dictates the significance of each step (i.e., whether a particular step is rate-limiting), not all intermediates are significantly populated at a given promoter, and additional intermediates not described here may be identifiable at other promoters. These kinetic differences allow regulators (as well as changes in growth conditions) to alter rates at target promoters without significantly affecting others (Haugen et al., 2008a) to generate the wide range of promoter strength *in vivo*.

### Mechanism of Promoter Melting

General models for the mechanism of RPo formation by  $E\sigma^{70}$  have been framed by two extremes that posit where duplex DNA unwinding occurs in RNAP (reviewed by Mazumder and Kapanidis, 2019), either outside (melt-load model) or inside the RNAP cleft (load-melt model). The melt-load model arose from analysis of bacterial RNAP-holoenzyme crystal structures (the only structures available until recently) that showed a closed-clamp conformation that could not accommodate duplex DNA (Vassilyev et al., 2002). It was thus proposed that duplex DNA positioned outside the cleft could unwind and only single-stranded DNA would be allowed into the RNAP cleft (Vassilyev et al., 2002).

The load-melt model is consistent with footprinting and other kinetic studies, primarily at  $\lambda P_R$ , that suggest that the ensemble of closed (i.e.,  $\text{KMnO}_4$  non-reactive) complexes includes complexes in which the duplex DNA downstream of the  $-10$  element is protected inside the RNAP cleft (Gries et al., 2010; Saecker et al., 2011). This model requires conformational changes in the RNAP to allow the entry of duplex DNA into the cleft. Early crystal structures defined a mobile structural element of the RNAP called the clamp, the opening of which would allow duplex DNA entry (Gnatt et al., 2001). Multiple conformational states of the RNAP clamp have been observed in solution by cryo-EM (Boyaci et al., 2018; Chen et al., 2019b) and single-molecule fluorescence resonance energy transfer (FRET) (Chakraborty et al.,

2012), which has also been used to observe clamp opening and closing dynamics directly (Duchi et al., 2018). It should be noted that conformational changes of the  $\beta$ lobe could also play a role in allowing DNA access to the RNAP cleft (Boyaci et al., 2019; Chen et al., 2010).

The results of this study, combined with other available evidence, support a combination of both models. Consistent with a melt-load model, the downstream duplex DNA in T-RPc (Figure 3) is located outside the cleft, and subsequent intermediates clearly show that transcription bubble nucleation occurs outside the cleft (T-RPi1, T-RPi1.5a; Figures 4C and 4D).

However, consistent with a load-melt model, the effects of antibiotics suggest a role for clamp dynamics in RPo formation (Boyaci et al., 2019; Feklistov et al., 2017; Lin et al., 2018; Srivastava et al., 2011). The RP2 intermediate observed with *Mtb* RNAP contains a partial bubble with the duplex DNA to be ultimately melted in RPo (including the transcription start site) enclosed in the RNAP cleft, indicating that final melting of the start site occurs within the RNAP cleft (Boyaci et al., 2019). Further structural characterization of RPo formation intermediates, now enabled by advances in cryo-EM, on diverse promoters and with and without transcription factors, will be required to further delineate the promoter melting mechanism.

## STAR★METHODS

Detailed methods are provided in the online version of this paper and include the following:

- KEY RESOURCES TABLE
- LEAD CONTACT AND MATERIALS AVAILABILITY
- EXPERIMENTAL MODEL AND SUBJECT DETAILS
- METHOD DETAILS
  - Protein Expression and Purification
  - Native mass spectrometry analysis
  - KMnO<sub>4</sub> and DNase I footprinting
  - *In vitro* transcription assays
  - Preparation of TraR-RNAP-DNA complexes for Cryo-EM
  - Cryo-EM grid preparation
  - Cryo-EM data acquisition and processing
  - Model building and refinement
- QUANTIFICATION AND STATISTICAL ANALYSIS
- DATA AND CODE AVAILABILITY

## SUPPLEMENTAL INFORMATION

Supplemental Information can be found online at <https://doi.org/10.1016/j.molcel.2020.02.017>.

## ACKNOWLEDGMENTS

We thank M. Ebrahim and J. Sotiris at The Rockefeller University Evelyn Gruss Lipper Cryo-electron Microscopy Resource Center for help with cryo-EM data collection and the members of the Darst/Campbell laboratory for helpful discussion on the manuscript. This work was supported by NIH grants P41 GM109824 and P41 GM103314 to B.T.C., R01 GM37048 to R.L.G., R01 GM114450 to E.A.C., and R35 GM118130 to S.A.D.

## AUTHOR CONTRIBUTIONS

J.C., C.C., S.G., A.Y.C., J.T.W., and M.F.M. expressed and purified proteins and performed biochemical assays. J.C., C.C., P.D.B.O., B.T.C., and R.M.S. performed the nMS analyses. J.C. and C.C. prepared the cryo-EM grids and collected the cryo-EM data. J.C. processed the cryo-EM data. J.C. and S.A.D. built, refined, and validated the models. B.T.C., W.R., R.L.G., E.A.C., and S.A.D. supervised the project. J.C., S.G., A.Y.C., R.M.S., W.R., R.L.G., E.A.C., and S.A.D. prepared and revised the manuscript.

## DECLARATION OF INTERESTS

The authors declare no competing interests.

Received: October 3, 2019

Revised: January 21, 2020

Accepted: February 19, 2020

Published: March 10, 2020

## SUPPORTING CITATIONS

The following reference appears in the Supplemental Information: Laskowski et al., 1993.

## REFERENCES

- Abascal-Palacios, G., Ramsay, E.P., Beuron, F., Morris, E., and Vannini, A. (2018). Structural basis of RNA polymerase III transcription initiation. *Nature* 553, 301–306.
- Adams, P.D., Afonine, P.V., Bunkóczi, G., Chen, V.B., Davis, I.W., Echols, N., Headd, J.J., Hung, L.-W., Kapral, G.J., Grosse-Kunstleve, R.W., et al. (2010). PHENIX: a comprehensive Python-based system for macromolecular structure solution. *Acta Crystallogr. D Biol. Crystallogr.* 66, 213–221.
- Afonine, P.V., Klaholz, B.P., Moriarty, N.W., Poon, B.K., Sobolev, O.V., Terwilliger, T.C., Adams, P.D., and Urzhumtsev, A. (2018). New tools for the analysis and validation of cryo-EM maps and atomic models. *Acta Crystallogr. D Struct. Biol.* 74, 814–840.
- Bae, B., Davis, E., Brown, D., Campbell, E.A., Wigneshweraraj, S., and Darst, S.A. (2013). Phage T7 Gp2 inhibition of Escherichia coli RNA polymerase involves misappropriation of  $\sigma^{70}$  domain 1.1. *Proc. Natl. Acad. Sci. USA* 110, 19772–19777.
- Bae, B., Feklistov, A., Lass-Napiorkowska, A., Landick, R., and Darst, S.A. (2015). Structure of a bacterial RNA polymerase holoenzyme open promoter complex. *eLife* 4, e08504.
- Baker, N.A., Sept, D., Joseph, S., Holst, M.J., and McCammon, J.A. (2001). Electrostatics of nanosystems: application to microtubules and the ribosome. *Proc. Natl. Acad. Sci. USA* 98, 10037–10041.
- Barker, M.M., Gaal, T., Josaitis, C.A., and Gourse, R.L. (2001). Mechanism of regulation of transcription initiation by ppGpp. I. Effects of ppGpp on transcription initiation in vivo and in vitro. *Journal of Molecular Biology* 305, 673–688.
- Bartlett, M.S., Gaal, T., Ross, W., and Gourse, R.L. (1998). RNA polymerase mutants that destabilize RNA polymerase-promoter complexes alter NTP-sensing by *rm* P1 promoters. *J. Mol. Biol.* 279, 331–345.
- Benoff, B., Yang, H., Lawson, C.L., Parkinson, G., Liu, J., Blatter, E., Ebricht, Y.W., Berman, H.M., and Ebricht, R.H. (2002). Structural basis of transcription activation: the CAP-alpha CTD-DNA complex. *Science* 297, 1562–1566.
- Blankschien, M.D., Potrykus, K., Grace, E., Choudhary, A., Vinella, D., Cashel, M., and Herman, C. (2009). TraR, a homolog of a RNAP secondary channel interactor, modulates transcription. *PLoS Genet.* 5, e1000345.
- Boyaci, H., Chen, J., Lilic, M., Palka, M., Mooney, R.A., Landick, R., Darst, S.A., and Campbell, E.A. (2018). Fidaxomicin jams *Mycobacterium tuberculosis* RNA polymerase motions needed for initiation via RbpA contacts. *eLife* 7, e34823.

- Boyaci, H., Chen, J., Jansen, R., Darst, S.A., and Campbell, E.A. (2019). Structures of an RNA polymerase promoter melting intermediate elucidate DNA unwinding. *Nature* **565**, 382–385.
- Buc, H., and McClure, W.R. (1985). Kinetics of open complex formation between *Escherichia coli* RNA polymerase and the lac UV5 promoter. Evidence for a sequential mechanism involving three steps. *Biochemistry* **24**, 2712–2723.
- Campbell, E.A., Muzzin, O., Chlenov, M., Sun, J.L., Olson, C.A., Weinman, O., Trester-Zedlitz, M.L., and Darst, S.A. (2002). Structure of the bacterial RNA polymerase promoter specificity sigma subunit. *Mol. Cell* **9**, 527–539.
- Cardone, G., Heymann, J.B., and Steven, A.C. (2013). One number does not fit all: mapping local variations in resolution in cryo-EM reconstructions. *J. Struct. Biol.* **184**, 226–236.
- Chakraborty, A., Wang, D., Ebright, Y.W., Korlann, Y., Kortkhonja, E., Kim, T., Chowdhury, S., Wigneshweraraj, S., Irschik, H., Jansen, R., et al. (2012). Opening and closing of the bacterial RNA polymerase clamp. *Science* **337**, 591–595.
- Chen, Y.F., and Helmann, J.D. (1997). DNA-melting at the *Bacillus subtilis* flagellin promoter nucleates near -10 and expands unidirectionally. *J. Mol. Biol.* **267**, 47–59.
- Chen, J., Darst, S.A., and Thirumalai, D. (2010). Promoter melting triggered by bacterial RNA polymerase occurs in three steps. *Proc. Natl. Acad. Sci. USA* **107**, 12523–12528.
- Chen, J., Wallarman, K.M., Feng, S., Leon, K., Feklistov, A., Winkelman, J.T., Zongli, L., Walz, T., Campbell, E.A., and Darst, S.A. (2017). 6S RNA mimics B-form DNA to regulate *Escherichia coli* RNA polymerase. *Molecular Cell* **68**, 388–397.e6.
- Chen, J., Noble, A.J., Kang, J.Y., and Darst, S.A. (2019a). Eliminating effects of particle adsorption to the air/water interface in single-particle cryo-electron microscopy - Bacterial RNA polymerase and CHAPSO. *J. Struct. Biol. X* **1**, 100005.
- Chen, J., Gopalkrishnan, S., Chiu, C., Chen, A.Y., Campbell, E.A., Gourse, R.L., Ross, W., and Darst, S.A. (2019b). *E. coli* TraR allosterically regulates transcription initiation by altering RNA polymerase conformation. *eLife* **8**, e49375.
- Duchi, D., Mazumder, A., Malinen, A.M., Ebright, R.H., and Kapanidis, A.N. (2018). The RNA polymerase clamp interconverts dynamically among three states and is stabilized in a partly closed state by ppGpp. *Nucleic Acids Res.* **46**, 7284–7295.
- Emsley, P., and Cowtan, K. (2004). Coot: model-building tools for molecular graphics. *Acta Crystallogr. D Biol. Crystallogr.* **60**, 2126–2132.
- Estrem, S.T., Gaal, T., Ross, W., and Gourse, R.L. (1998). Identification of an UP element consensus sequence for bacterial promoters. *Proc. Natl. Acad. Sci. USA* **95**, 9761–9766.
- Feklistov, A., and Darst, S.A. (2011). Structural basis for promoter-10 element recognition by the bacterial RNA polymerase  $\sigma$  subunit. *Cell* **147**, 1257–1269.
- Feklistov, A., Sharon, B.D., Darst, S.A., and Gross, C.A. (2014). Bacterial sigma factors: a historical, structural, and genomic perspective. *Annu. Rev. Microbiol.* **68**, 357–376.
- Feklistov, A., Bae, B., Hauver, J., Lass-Napiorkowska, A., Kalesse, M., Glaus, F., Altmann, K.-H., Heyduk, T., Landick, R., and Darst, S.A. (2017). RNA polymerase motions during promoter melting. *Science* **356**, 863–866.
- Galburt, E.A. (2018). The calculation of transcript flux ratios reveals single regulatory mechanisms capable of activation and repression. *Proc. Natl. Acad. Sci. USA* **115**, E11604–E11613.
- Gnatt, A.L., Cramer, P., Fu, J., Bushnell, D.A., and Kornberg, R.D. (2001). Structural basis of transcription: an RNA polymerase II elongation complex at 3.3 Å resolution. *Science* **292**, 1876–1882.
- Gopalkrishnan, S., Ross, W., Chen, A.Y., and Gourse, R.L. (2017). TraR directly regulates transcription initiation by mimicking the combined effects of the global regulators DksA and ppGpp. *Proc. Natl. Acad. Sci. USA* **114**, E5539–E5548.
- Gourse, R.L., Chen, A.Y., Gopalkrishnan, S., Sanchez-Vazquez, P., Myers, A., and Ross, W. (2018). Transcriptional Responses to ppGpp and DksA. *Annu. Rev. Microbiol.* **72**, 163–184.
- Gries, T.J., Kontur, W.S., Capp, M.W., Saecker, R.M., and Record, M.T., Jr. (2010). One-step DNA melting in the RNA polymerase cleft opens the initiation bubble to form an unstable open complex. *Proc. Natl. Acad. Sci. USA* **107**, 10418–10423.
- Gruber, T.M., and Bryant, D.A. (1997). Molecular systematic studies of eubacteria, using sigma70-type sigma factors of group 1 and group 2. *J. Bacteriol.* **179**, 1734–1747.
- Gruber, T.M., and Gross, C.A. (2003). Multiple sigma subunits and the partitioning of bacterial transcription space. *Annu. Rev. Microbiol.* **57**, 441–466.
- Haugen, S.P., Berkmen, M.B., Ross, W., Gaal, T., Ward, C., and Gourse, R.L. (2006). rRNA promoter regulation by nonoptimal binding of  $\sigma$  region 1.2: an additional recognition element for RNA polymerase. *Cell* **125**, 1069–1082.
- Haugen, S.P., Ross, W., and Gourse, R.L. (2008a). Advances in bacterial promoter recognition and its control by factors that do not bind DNA. *Nat. Rev. Microbiol.* **6**, 507–519.
- Haugen, S.P., Ross, W., Manrique, M., and Gourse, R.L. (2008b). Fine structure of the promoter-sigma region 1.2 interaction. *Proc. Natl. Acad. Sci. USA* **105**, 3292–3297.
- Hawley, D.K., and McClure, W.R. (1982). Mechanism of activation of transcription initiation from the lambda PRM promoter. *J. Mol. Biol.* **157**, 493–525.
- He, Y., Fang, J., Taatjes, D.J., and Nogales, E. (2013). Structural visualization of key steps in human transcription initiation. *Nature* **495**, 481–486.
- He, Y., Yan, C., Fang, J., Inouye, C., Tjian, R., Ivanov, I., and Nogales, E. (2016). Near-atomic resolution visualization of human transcription promoter opening. *Nature* **533**, 359–365.
- Heyduk, E., Kuznedelov, K., Severinov, K., and Heyduk, T. (2006). A consensus adenine at position -11 of the nontemplate strand of bacterial promoter is important for nucleation of promoter melting. *J. Biol. Chem.* **281**, 12362–12369.
- Hubin, E.A., Fay, A., Xu, C., Bean, J.M., Saecker, R.M., Glickman, M.S., Darst, S.A., and Campbell, E.A. (2017a). Structure and function of the mycobacterial transcription initiation complex with the essential regulator RbpA. *eLife* **6**, e22520.
- Hubin, E.A., Lilic, M., Darst, S.A., and Campbell, E.A. (2017b). Structural insights into the mycobacteria transcription initiation complex from analysis of X-ray crystal structures. *Nat. Commun.* **8**, 16072.
- Kadesch, T.R., Rosenberg, S., and Chamberlin, M.J. (1982). Binding of *Escherichia coli* RNA polymerase holoenzyme to bacteriophage T7 DNA. Measurements of binding at bacteriophage T7 promoter A1 using a template competition assay. *J. Mol. Biol.* **155**, 1–29.
- Kontur, W.S., Saecker, R.M., Capp, M.W., and Record, M.T., Jr. (2008). Late steps in the formation of *E. coli* RNA polymerase-lambda P R promoter open complexes: characterization of conformational changes by rapid [perturbant] upshift experiments. *J. Mol. Biol.* **376**, 1034–1047.
- Kontur, W.S., Capp, M.W., Gries, T.J., Saecker, R.M., and Record, M.T., Jr. (2010). Probing DNA binding, DNA opening, and assembly of a downstream clamp/jaw in *Escherichia coli* RNA polymerase-lambdaP(R) promoter complexes using salt and the physiological anion glutamate. *Biochemistry* **49**, 4361–4373.
- Kovacic, R.T. (1987). The 0 degree C closed complexes between *Escherichia coli* RNA polymerase and two promoters, T7-A3 and lacUV5. *J. Biol. Chem.* **262**, 13654–13661.
- Krissinel, E., and Henrick, K. (2007). Inference of macromolecular assemblies from crystalline state. *J. Mol. Biol.* **372**, 774–797.
- Lane, W.J., and Darst, S.A. (2010). Molecular evolution of multisubunit RNA polymerases: sequence analysis. *J. Mol. Biol.* **395**, 671–685.
- Laskowski, R.A., MacArthur, M.W., Moss, D.S., Thornton, J.M., and Cr, I.U. (1993). PROCHECK: a program to check the stereochemical quality of protein structures. *J. Appl. Cryst.* **26**, 283–291.

- Lee, D.J., Minchin, S.D., and Busby, S.J.W. (2012). Activating transcription in bacteria. *Annu. Rev. Microbiol.* **66**, 125–152.
- Lemke, J.J., Sanchez-Vazquez, P., Burgos, H.L., Hedberg, G., Ross, W., and Gourse, R.L. (2011). Direct regulation of *Escherichia coli* ribosomal protein promoters by the transcription factors ppGpp and DksA. *Proc. Natl. Acad. Sci. USA* **108**, 5712–5717.
- Lim, H.M., Lee, H.J., Roy, S., and Adhya, S. (2001). A “master” in base unpairing during isomerization of a promoter upon RNA polymerase binding. *Proc. Natl. Acad. Sci. USA* **98**, 14849–14852.
- Lin, W., Das, K., Degen, D., Mazumder, A., Duchi, D., Wang, D., Ebright, Y.W., Ebright, R.Y., Sineva, E., Gigliotti, M., et al. (2018). Structural Basis of Transcription Inhibition by Fidaxomicin (Lipiarmycin A3). *Mol. Cell* **70**, 60–71.e15.
- Marty, M.T., Baldwin, A.J., Marklund, E.G., Hochberg, G.K.A., Benesch, J.L.P., and Robinson, C.V. (2015). Bayesian deconvolution of mass and ion mobility spectra: from binary interactions to polydisperse ensembles. *Anal. Chem.* **87**, 4370–4376.
- Mastrorade, D.N. (2005). Automated electron microscope tomography using robust prediction of specimen movements. *J. Struct. Biol.* **152**, 36–51.
- Mazumder, A., and Kapanidis, A.N. (2019). Recent Advances in Understanding  $\sigma$ 70-Dependent Transcription Initiation Mechanisms. *J. Mol. Biol.* **431**, 3947–3959.
- McClure, W.R. (1985). Mechanism and control of transcription initiation in prokaryotes. *Annu. Rev. Biochem.* **54**, 171–204.
- Mekler, V., Kortkhonjia, E., Mukhopadhyay, J., Knight, J., Revyakin, A., Kapanidis, A.N., Niu, W., Ebright, Y.W., Levy, R., and Ebright, R.H. (2002). Structural organization of bacterial RNA polymerase holoenzyme and the RNA polymerase-promoter open complex. *Cell* **108**, 599–614.
- Morin, A., Eisenbraun, B., Key, J., Sanschagrín, P.C., Timony, M.A., Ottaviano, M., and Sliz, P. (2013). Collaboration gets the most out of software. *eLife* **2**, e01456.
- Nagy, J., Grohmann, D., Cheung, A.C.M., Schulz, S., Smollett, K., Werner, F., and Michaelis, J. (2015). Complete architecture of the archaeal RNA polymerase open complex from single-molecule FRET and NPS. *Nat. Commun.* **6**, 6161.
- Narayanan, A., Vago, F.S., Li, K., Qayyum, M.Z., Yernool, D., Jiang, W., and Murakami, K.S. (2018). Cryo-EM structure of *Escherichia coli*  $\sigma$ 70 RNA polymerase and promoter DNA complex revealed a role of  $\sigma$  non-conserved region during the open complex formation. *J. Biol. Chem.* **293**, 7367–7375.
- Olinares, P.D.B., Dunn, A.D., Padovan, J.C., Fernandez-Martinez, J., Rout, M.P., and Chait, B.T. (2016). A Robust Workflow for Native Mass Spectrometric Analysis of Affinity-Isolated Endogenous Protein Assemblies. *Anal. Chem.* **88**, 2799–2807.
- Pettersen, E.F., Goddard, T.D., Huang, C.C., Couch, G.S., Greenblatt, D.M., Meng, E.C., and Ferrin, T.E. (2004). UCSF Chimera—a visualization system for exploratory research and analysis. *J. Comput. Chem.* **25**, 1605–1612.
- Plaschka, C., Hantsche, M., Dienemann, C., Burzinski, C., Plitzko, J., and Cramer, P. (2016). Transcription initiation complex structures elucidate DNA opening. *Nature* **533**, 353–358.
- Punjani, A., Rubinstein, J.L., Fleet, D.J., and Brubaker, M.A. (2017). cryoSPARC: algorithms for rapid unsupervised cryo-EM structure determination. *Nat. Methods* **14**, 290–296.
- Reid, D.J., Diesing, J.M., Miller, M.A., Perry, S.M., Wales, J.A., Montfort, W.R., and Marty, M.T. (2019). MetaUniDec: High-Throughput Deconvolution of Native Mass Spectra. *J. Am. Soc. Mass Spectrom.* **30**, 118–127.
- Roe, J.H., Burgess, R.R., and Record, M.T., Jr. (1984). Kinetics and mechanism of the interaction of *Escherichia coli* RNA polymerase with the lambda PR promoter. *J. Mol. Biol.* **176**, 495–522.
- Rogozina, A., Zaychikov, E., Buckle, M., Heumann, H., and Sclavi, B. (2009). DNA melting by RNA polymerase at the T7A1 promoter precedes the rate-limiting step at 37 degrees C and results in the accumulation of an off-pathway intermediate. *Nucleic Acids Res.* **37**, 5390–5404.
- Rohou, A., and Grigorieff, N. (2015). CTFFIND4: fast and accurate defocus estimation from electron micrographs. *J. Struct. Biol.* **192**, 216–221.
- Rosenberg, S., Kadesch, T.R., and Chamberlin, M.J. (1982). Binding of *Escherichia coli* RNA polymerase holoenzyme to bacteriophage T7 DNA. Measurements of the rate of open complex formation at T7 promoter A. *J. Mol. Biol.* **155**, 31–51.
- Ross, W., and Gourse, R.L. (2005). Sequence-independent upstream DNA-alphaCTD interactions strongly stimulate *Escherichia coli* RNA polymerase-lacUV5 promoter association. *Proc. Natl. Acad. Sci. USA* **102**, 291–296.
- Ross, W., and Gourse, R.L. (2009). Analysis of RNA polymerase-promoter complex formation. *Methods* **47**, 13–24.
- Ross, W., Gosink, K.K., Salomon, J., Igarashi, K., Zou, C., Ishihama, A., Severinov, K., and Gourse, R.L. (1993). A third recognition element in bacterial promoters: DNA binding by the alpha subunit of RNA polymerase. *Science* **262**, 1407–1413.
- Ross, W., Ernst, A., and Gourse, R.L. (2001). Fine structure of *E. coli* RNA polymerase-promoter interactions: alpha subunit binding to the UP element minor groove. *Genes Dev.* **15**, 491–506.
- Ross, W., Schneider, D.A., Paul, B.J., Mertens, A., and Gourse, R.L. (2003). An intersubunit contact stimulating transcription initiation by *E. coli* RNA polymerase: interaction of the alpha C-terminal domain and sigma region 4. *Genes Dev.* **17**, 1293–1307.
- Ross, W., Thompson, J.F., Newlands, J.T., and Gourse, R.L. (1990). *E. coli* Fis protein activates ribosomal RNA transcription in vitro and in vivo. *The EMBO Journal* **9**, 3733–3742.
- Ruff, E.F., Record, M.T., Jr., and Artsimovitch, I. (2015). Initial events in bacterial transcription initiation. *Biomolecules* **5**, 1035–1062.
- Rutherford, S.T., Villers, C.L., Lee, J.-H., Ross, W., and Gourse, R.L. (2009). Allosteric control of *Escherichia coli* rRNA promoter complexes by DksA. *Genes Dev.* **23**, 236–248.
- Saecker, R.M., Record, M.T., Jr., and Dehaseth, P.L. (2011). Mechanism of bacterial transcription initiation: RNA polymerase - promoter binding, isomerization to initiation-competent open complexes, and initiation of RNA synthesis. *J. Mol. Biol.* **412**, 754–771.
- Sanchez-Vazquez, P., Dewey, C.N., Kitten, N., Ross, W., and Gourse, R.L. (2019). Genome-wide effects on *Escherichia coli* transcription from ppGpp binding to its two sites on RNA polymerase. *Proc. Natl. Acad. Sci. USA* **116**, 8310–8319.
- Scheres, S.H.W. (2012). RELION: implementation of a Bayesian approach to cryo-EM structure determination. *J. Struct. Biol.* **180**, 519–530.
- Schickor, P., Metzger, W., Werel, W., Lederer, H., and Heumann, H. (1990). Topography of intermediates in transcription initiation of *E. coli*. *EMBO J.* **9**, 2215–2220.
- Schulz, S., Gietl, A., Smollett, K., Tinnefeld, P., Werner, F., and Grohmann, D. (2016). TFE and Spt4/5 open and close the RNA polymerase clamp during the transcription cycle. *Proc. Natl. Acad. Sci. USA* **113**, E1816–E1825.
- Sclavi, B., Zaychikov, E., Rogozina, A., Walther, F., Buckle, M., and Heumann, H. (2005). Real-time characterization of intermediates in the pathway to open complex formation by *Escherichia coli* RNA polymerase at the T7A1 promoter. *Proc. Natl. Acad. Sci. USA* **102**, 4706–4711.
- Shultzaberger, R.K., Chen, Z., Lewis, K.A., and Schneider, T.D. (2007). Anatomy of *Escherichia coli* sigma70 promoters. *Nucleic Acids Res.* **35**, 771–788.
- Srivastava, A., Talaue, M., Liu, S., Degen, D., Ebright, R.Y., Sineva, E., Chakraborty, A., Druzhinin, S.Y., Chatterjee, S., Mukhopadhyay, J., et al. (2011). New target for inhibition of bacterial RNA polymerase: ‘switch region’. *Curr. Opin. Microbiol.* **14**, 532–543.
- Svetlov, V., and Artsimovitch, I. (2015). Purification of bacterial RNA polymerase: tools and protocols. *Methods Mol. Biol.* **1276**, 13–29.
- Tafur, L., Sadian, Y., Hoffmann, N.A., Jakobi, A.J., Wetzler, R., Hagen, W.J.H., Sachse, C., and Müller, C.W. (2016). Molecular Structures of Transcribing RNA Polymerase I. *Mol. Cell* **64**, 1135–1143.

- Twist, K.-A., Husnain, S.I., Franke, J.D., Jain, D., Campbell, E.A., Nickels, B.E., Thomas, M.S., Darst, S.A., and Westblade, L.F. (2011). A novel method for the production of in vivo-assembled, recombinant *Escherichia coli* RNA polymerase lacking the  $\alpha$  C-terminal domain. *Protein Science* 20, 986–995.
- Vassilyev, D.G., Sekine, S., Laptenko, O., Lee, J., Vassilyeva, M.N., Borukhov, S., and Yokoyama, S. (2002). Crystal structure of a bacterial RNA polymerase holoenzyme at 2.6 Å resolution. *Nature* 417, 712–719.
- Vassilyev, D.G., Vassilyeva, M.N., Zhang, J., Palangat, M., Artsimovitch, I., and Landick, R. (2007). Structural basis for substrate loading in bacterial RNA polymerase. *Nature* 448, 163–168.
- Vorländer, M.K., Khatter, H., Wetzell, R., Hagen, W.J.H., and Müller, C.W. (2018). Molecular mechanism of promoter opening by RNA polymerase III. *Nature* 553, 295–300.
- Walter, G., Zillig, W., Palm, P., and Fuchs, E. (1967). Initiation of DNA-dependent RNA synthesis and the effect of heparin on RNA polymerase. *Eur. J. Biochem.* 3, 194–201.
- Wang, D., Bushnell, D.A., Westover, K.D., Kaplan, C.D., and Kornberg, R.D. (2006). Structural basis of transcription: role of the trigger loop in substrate specificity and catalysis. *Cell* 127, 941–954.
- Windgassen, T.A., Mooney, R.A., Nayak, D., Palangat, M., Zhang, J., and Landick, R. (2014). Trigger-helix folding pathway and SI3 mediate catalysis and hairpin-stabilized pausing by *Escherichia coli* RNA polymerase. *Nucleic Acids Res.* 42, 12707–12721.
- Winkelman, J.T., Winkelman, B.T., Boyce, J., Maloney, M.F., Chen, A.Y., Ross, W., and Gourse, R.L. (2015). Crosslink Mapping at Amino Acid-Base Resolution Reveals the Path of Scrunched DNA in Initial Transcribing Complexes. *Mol. Cell* 59, 768–780.
- Winkelman, J.T., Chandrangsu, P., Ross, W., and Gourse, R.L. (2016). Open complex scrunching before nucleotide addition accounts for the unusual transcription start site of *E. coli* ribosomal RNA promoters. *Proc. Natl. Acad. Sci. USA* 113, E1787–E1795.
- Yuzenkova, Y., Tadigotla, V.R., Severinov, K., and Zenkin, N. (2011). A new basal promoter element recognized by RNA polymerase core enzyme. *EMBO J.* 30, 3766–3775.
- Zhang, K. (2016). Gctf: real-time CTF determination and correction. *J. Struct. Biol.* 193, 1–12.
- Zhang, Y., Feng, Y., Chatterjee, S., Tuske, S., Ho, M.X., Arnold, E., and Ebright, R.H. (2012). Structural basis of transcription initiation. *Science* 338, 1076–1080.
- Zheng, S.Q., Palovcak, E., Armache, J.-P., Verba, K.A., Cheng, Y., and Agard, D.A. (2017). MotionCor2: anisotropic correction of beam-induced motion for improved cryo-electron microscopy. *Nat. Methods* 14, 331–332.
- Zivanov, J., Nakane, T., Forsberg, B.O., Kimanius, D., Hagen, W.J., Lindahl, E., and Scheres, S.H.W. (2018). New tools for automated high-resolution cryo-EM structure determination in RELION-3. *eLife* 7, e42166.
- Zuo, Y., and Steitz, T.A. (2015). Crystal structures of the *E. coli* transcription initiation complexes with a complete bubble. *Mol. Cell* 58, 534–540.

## STAR★METHODS

### KEY RESOURCES TABLE

REAGENT or RESOURCE	SOURCE	IDENTIFIER
<b>Bacterial and Virus Strains</b>		
<i>E. coli</i> BL21(DE3)	EMD Millipore	N/A
<b>Chemicals, Peptides, and Recombinant Proteins</b>		
3-[[3-Cholamidopropyl]dimethylammonio]-2-hydroxy-1-propanesulfonate (CHAPSO)	Anatrace	Cat# C317
<i>E. coli</i> RNAP (cryo-EM samples)	<a href="#">Chen et al., 2019b</a>	N/A
<i>E. coli</i> RNAP, WT (Biochemistry)	<a href="#">Svetlov and Artsimovitch, 2015</a>	N/A
<i>E. coli</i> RNAP, $\beta$ A474L	This paper	N/A
<i>E. coli</i> RNAP, $\beta$ A474V	This paper	N/A
<i>E. coli</i> RNAP, $\beta$ R378A	This paper	N/A
<i>E. coli</i> RNAP, $\beta$ R378E	This paper	N/A
<i>E. coli</i> RNAP, $\beta$ R378E $\beta$ R394E	This paper	N/A
<i>E. coli</i> RNAP, $\beta$ R394A	This paper	N/A
<i>E. coli</i> RNAP, $\beta$ R394E	This paper	N/A
Polyethyleneimine	Fisher Scientific	Cat# AC178572500
<b>Deposited Data</b>		
Coordinates of <i>E. coli</i> $E\sigma^{70}$	<a href="#">Chen et al., 2019b</a>	PDB: 6P1K
Coordinates of <i>E. coli</i> $E\sigma^{70}$ /Wt <i>rpsT</i> P2	<a href="#">Chen et al., 2019b</a>	PDB: 6OUL
Coordinates of <i>E. coli</i> TraR/ $E\sigma^{70}$ (I)	<a href="#">Chen et al., 2019b</a>	PDB: 6N57
Coordinates of <i>E. coli</i> TraR/ $E\sigma^{70}$ (II)	<a href="#">Chen et al., 2019b</a>	PDB: 6N58
Coordinates of <i>E. coli</i> TraR/ $E\sigma^{70}$ /Wt <i>rpsT</i> P2 (T-preRPO)	This paper	PDB: 6PSV
Coordinates of <i>E. coli</i> TraR/ $E\sigma^{70}$ /Wt <i>rpsT</i> P2 (T-RPc)	This paper	PDB: 6PSQ
Coordinates of <i>E. coli</i> TraR/ $E\sigma^{70}$ /Wt <i>rpsT</i> P2 (T-RPi1)	This paper	PDB: 6PSR
Coordinates of <i>E. coli</i> TraR/ $E\sigma^{70}$ /Wt <i>rpsT</i> P2 (T-RPi2)	This paper	PDB: 6PSU
Coordinates of <i>E. coli</i> TraR/ $E\sigma^{70}$ /Wt <i>rpsT</i> P2 (T-RPo)	This paper	PDB: 6PSW
Coordinates of <i>E. coli</i> TraR/ $E\sigma^{70}$ /Wt <i>rpsT</i> P2* (T-RPi1.5a)	This paper	PDB: 6PSS
Coordinates of <i>E. coli</i> TraR/ $E\sigma^{70}$ /Wt <i>rpsT</i> P2* (T-RPi1.5b)	This paper	PDB: 6PST
Cryo-EM map of <i>E. coli</i> TraR/ $E\sigma^{70}$ / <i>rpsT</i> P2* (T-RPi1.5a)	This paper	EMD_20462
Cryo-EM map of <i>E. coli</i> TraR/ $E\sigma^{70}$ /Wt <i>rpsT</i> P2 (T-preRPO)	This paper	EMD-20465
Cryo-EM map of <i>E. coli</i> TraR/ $E\sigma^{70}$ /Wt <i>rpsT</i> P2 (T-RPc)	This paper	EMD-20460
Cryo-EM map of <i>E. coli</i> TraR/ $E\sigma^{70}$ /Wt <i>rpsT</i> P2 (T-RPi1)	This paper	EMD-20461
Cryo-EM map of <i>E. coli</i> TraR/ $E\sigma^{70}$ /Wt <i>rpsT</i> P2 (T-RPi2)	This paper	EMD-20464
Cryo-EM map of <i>E. coli</i> TraR/ $E\sigma^{70}$ /Wt <i>rpsT</i> P2 (T-RPo)	This paper	EMD-20466
Cryo-EM map of <i>E. coli</i> TraR/ $E\sigma^{70}$ /Wt <i>rpsT</i> P2* (T-RPi1.5b)	This paper	EMD-20463
<b>Experimental Models: Organisms/Strains</b>		
<i>Escherichia coli</i>	N/A	N/A
<b>Oligonucleotides</b>		
pIA900 $\beta$ A474L: gtgtagagcgtCTggtgaaagagcgtc	This paper, IDT	N/A
pIA900 $\beta$ A474V: gtgtagagcgtgTggtgaaagagcgtc	This paper, IDT	N/A
pIA900 $\beta$ R378A: gagccgccgactGCCgaagcagctgaaagcctg	This paper, IDT	N/A
pIA900 $\beta$ R378E: gagccgccgactGAAgaagcagctgaaagcctg	This paper, IDT	N/A
pIA900 $\beta$ R394A: cttctccgaagacGcttatgacttgctgc	This paper, IDT	N/A
pIA900 $\beta$ R394E: cttctccgaagacGAAatgacttgctgc	This paper, IDT	N/A

(Continued on next page)

**Continued**

REAGENT or RESOURCE	SOURCE	IDENTIFIER
rpsTP2(−60to+25)_{-11/-10CG_bot: 5′-GCG TTC TAT ATG GAC AAT TCA AAG GCC GAG GAA TGC GCC CTT TTA GCC TTC TTT TGT CAA TGG ATT TGT GCA AAT AAG CGC CGC C-3′	This paper, IDT	N/A
rpsTP2(−60to+25)_{(T-7A)_top: 5′-GGC GGC GCT TAT TTG CAC AAA TCC ATT GAC AAA AGA AGG CTA AAA GGG CAT ATA CCT CGG CCT TTG AAT TGT CCA TAT AGA ACG C-3′	This paper, IDT	N/A
rpsTP2(−60to+25)_{bot: 5′-GCG TTC TAT ATG GAC AAT TCA AAG GCC GAG GAA TAT GCC CTT TTA GCC TTC TTT TGT CAA TGG ATT TGT GCA AAT AAG CGC CGC C-3′	This paper, IDT	N/A
rpsTP2(−60to+25)_{top: 5′-GGC GGC GCT TAT TTG CAC AAA TCC ATT GAC AAA AGA AGG CTA AAA GGG CAT ATT CCT CGG CCT TTG AAT TGT CCA TAT AGA ACG C-3′	This paper, IDT	N/A
<b>Recombinant DNA</b>		
<i>E. coli</i> RNAP, pIA900 WT	<a href="#">Svetlov and Artsimovitch, 2015</a>	N/A
<i>E. coli</i> RNAP, pIA900 βA474L	This paper	pRLG15445
<i>E. coli</i> RNAP, pIA900 βA474V	This paper	pRLG15444
<i>E. coli</i> RNAP, pIA900 βR378A	This paper	pRLG15446
<i>E. coli</i> RNAP, pIA900 βR378E	This paper	pRLG15447
<i>E. coli</i> RNAP, pIA900 βR378E βR394E	This paper	pRLG15450
<i>E. coli</i> RNAP, pIA900 βR394A	This paper	pRLG15448
<i>E. coli</i> RNAP, pIA900 βR394E	This paper	pRLG15449
p770	<a href="#">Ross et al., 1990</a>	pRLG770
p770- <i>rpsT</i> P2 (−89 to +50)	<a href="#">Lemke et al., 2011</a>	pRLG14658
p770- <i>rrmB</i> P1 (−88 to +50)	<a href="#">Ross et al., 1990</a>	pRLG13065
p770- <i>thrABC</i> (−72 to +16)	<a href="#">Barker et al., 2001</a>	pRLG15276
pACYCDuet-1_Ec_rpoZ	<a href="#">Twist et al., 2011</a>	N/A
pEcrpoABC(-XH)Z	<a href="#">Twist et al., 2011</a>	N/A
pET28a	EMD Millipore	N/A
pET28a-His <sub>10</sub> -SUMO rpoD	<a href="#">Chen et al., 2017</a>	N/A
pET28a-His <sub>10</sub> -SUMO traR	<a href="#">Chen et al., 2019b</a>	pRLG15142
pIA900, multisubunit RNAP plasmid	<a href="#">Svetlov and Artsimovitch, 2015</a>	N/A
pSL6- <i>rpsT</i> P2 (−68 to +50)	<a href="#">Gopalkrishnan et al., 2017</a>	pRLG11272
pSL6- <i>rpsT</i> P2 (−68 to +50) (T-7A)	This paper	pRLG12844
<b>Software and Algorithms</b>		
Bayesian Polishing	<a href="#">Zivanov et al., 2018</a>	<a href="https://github.com/3dem/reliion">https://github.com/3dem/reliion</a>
bloclift	<a href="#">Cardone et al., 2013</a>	<a href="https://lsbr.niams.nih.gov/bsoft/programs/blocres.html">https://lsbr.niams.nih.gov/bsoft/programs/blocres.html</a>
blocres	<a href="#">Cardone et al., 2013</a>	<a href="https://lsbr.niams.nih.gov/bsoft/programs/blocres.html">https://lsbr.niams.nih.gov/bsoft/programs/blocres.html</a>
Coot	<a href="#">Emsley and Cowtan, 2004</a>	<a href="https://www2.mrc-lmb.cam.ac.uk/personal/pemsley/coot">https://www2.mrc-lmb.cam.ac.uk/personal/pemsley/coot</a>
cryoSPARC	<a href="#">Punjani et al., 2017</a>	<a href="https://cryosparc.com/">https://cryosparc.com/</a>
CTFFIND4	<a href="#">Rohou and Grigorieff, 2015</a>	<a href="https://grigoriefflab.janelia.org/ctffind4">https://grigoriefflab.janelia.org/ctffind4</a>
Gautomatch	N/A	<a href="https://www.mrc-lmb.cam.ac.uk/kzhang/Gautomatch/">https://www.mrc-lmb.cam.ac.uk/kzhang/Gautomatch/</a>
Gctf	<a href="#">Zhang, 2016</a>	<a href="https://www.mrc-lmb.cam.ac.uk/kzhang/Gctf/">https://www.mrc-lmb.cam.ac.uk/kzhang/Gctf/</a>

(Continued on next page)

**Continued**

REAGENT or RESOURCE	SOURCE	IDENTIFIER
GraphPad Prism	GraphPad	<a href="http://www.graphpad.com/scientific-software/prism/">http://www.graphpad.com/scientific-software/prism/</a>
ImageQuant 5.2	GE Healthcare, Pittsburgh PA	N/A
m/z- Knexus edition	Proteometrics, LLC	N/A
Molprobrity	Chen et al., 2010	<a href="http://molprobrity.biochem.duke.edu">http://molprobrity.biochem.duke.edu</a>
MotionCor2	Zheng et al., 2017	N/A
MTRIAGE	Afonine et al., 2018	<a href="https://www.phenix-online.org/documentation/reference/mtriage.html">https://www.phenix-online.org/documentation/reference/mtriage.html</a>
PDBePISA	Krissinel and Henrick, 2007	<a href="https://www.ebi.ac.uk/pdbe/pisa/">https://www.ebi.ac.uk/pdbe/pisa/</a>
PHENIX	Adams et al., 2010	<a href="https://www.phenix-online.org/documentation/index.html">https://www.phenix-online.org/documentation/index.html</a>
Qual Browser Thermo Xcalibur version 3.0.63	Thermo Fisher Scientific Inc.	Thermo Scientific MS instruments
RELION	Scheres, 2012	<a href="https://github.com/3dem/relion">https://github.com/3dem/relion</a>
SBGrid	Morin et al., 2013	<a href="https://sbgrid.org/">https://sbgrid.org/</a>
SerialEM	Mastronarde, 2005	<a href="http://bio3d.colorado.edu/SerialEM">http://bio3d.colorado.edu/SerialEM</a>
The PyMOL Molecular Graphics System	Schrödinger, LLC	<a href="https://pymol.org/2/">https://pymol.org/2/</a>
UCSF Chimera	Pettersen et al., 2004	<a href="https://www.cgl.ucsf.edu/chimera">https://www.cgl.ucsf.edu/chimera</a>
UniDec version 3.2	Marty et al., 2015	<a href="https://github.com/michaelmarty/UniDec/releases">https://github.com/michaelmarty/UniDec/releases</a>
<b>Other</b>		
Bio-Rex 70 cation exchange resin, analytical grade, 100-200 mesh	Bio-Rad	Cat# 1425842
C-flat CF-1.2/1.3 400 mesh gold grids	Electron Microscopy Sciences	Cat# CF413-100-Au
HiLoad 26/600 Superdex 200 pg	GE Healthcare Life Sciences	Cat# 28989336
HiTrap IMAC HP	GE Healthcare Life Sciences	Cat# 17092003
Isotope [ $\alpha$ - $^{32}$ P]UTP	Perkin Elmer	Cat # BLU507H500UCI
Isotope [ $\alpha$ - $^{32}$ P]-dCTP	Perkin Elmer	Cat # BLU013H250UCI
Superose 6 INCREASE 10/300 GL	GE Healthcare Life Sciences	Cat# 29091596
Zeba Micro Spin Desalting Columns, 40K MWCO	Thermo Pierce	Cat. # 87765

**LEAD CONTACT AND MATERIALS AVAILABILITY**

All unique/stable reagents generated in this study are available without restriction from the Lead Contact, Seth A. Darst ([darst@rockefeller.edu](mailto:darst@rockefeller.edu)).

**EXPERIMENTAL MODEL AND SUBJECT DETAILS**

RNAP core ( $\alpha_2\beta\beta'\omega$ ),  $\sigma^{70}$ , and TraR are proteins found in *Eco*. For protein expression, *Eco* BL21(DE3) [*Eco* str. B F<sup>-</sup> *ompT gal dcm lon hsdS<sub>B</sub>(r<sub>B</sub><sup>-</sup>m<sub>B</sub><sup>-</sup>)*  $\lambda$ (DE3 [*lacI lacUV5-T7p07 ind1 sam7 nin5*]) [*malB<sup>+</sup>*]<sub>K-12</sub>( $\lambda^S$ )] was used.

**METHOD DETAILS**

**Protein Expression and Purification**

*Eco* RNAP (harboring full-length  $\alpha$ -subunits),  $\sigma^{70}$ , and TraR were purified as described previously (Chen et al., 2019b). A pET-based plasmid overexpressing each subunit of *Eco* RNAP (full-length  $\alpha$ ,  $\beta$ ,  $\omega$ ) as well as  $\beta'$ -PPX-His10 (PPX; PreScission protease site, LEVLFQGP, GE Healthcare) was co-transformed with a pACYCDuet-1 plasmid containing *Eco* rpoZ (encoding  $\omega$ ) into *Eco* BL21(DE3) (Novagen). Protein expression was induced with 1 mM isopropyl  $\beta$ -D-thiogalactopyranoside (IPTG) for 4 hr at 30°C. Cells were harvested and lysed with a French Press (Avestin) at 4°C. Lysate was precipitated using polyethyleneimine [PEI, 10% (w/v), pH 8.0, Acros Organics]. Pellets were washed and RNAP was eluted. The PEI elutions were precipitated with ammonium sulfate. Pellets were harvested, resuspended and loaded on to HiTrap IMAC HP columns (GE Healthcare Life Sciences) for purification by nickel affinity chromatography. Bound RNAP was washed on column, eluted and dialyzed. Dialyzed RNAP was loaded onto a

Biorex-70 column (Bio-Rad) for purification by ion exchange chromatography. Eluted RNAP was concentrated by centrifugal filtration, then loaded onto a HiLoad 26/600 Superdex 200 column (GE Healthcare Life Sciences) for purification by size exclusion chromatography. Purified RNAP was supplemented with glycerol to 20% (v/v), flash frozen in liquid N<sub>2</sub>, and stored at –80°C.

*Eco*  $\sigma^{70}$  was purified as described previously (Chen et al., 2019b). Plasmid encoding *Eco* His<sub>10</sub>-SUMO- $\sigma^{70}$  was transformed into *Eco* BL21(DE3) (Novagen). Protein expression was induced with 1 mM IPTG for 1 hr at 30°C. Cells were harvested and lysed with a French Press (Avestin) at 4°C. Lysate was loaded onto a HiTrap IMAC HP column (GE Healthcare Life Sciences) for purification by nickel affinity chromatography. Eluted  $\sigma^{70}$  was cleaved with ULPI SUMO protease (Thermo Fisher Scientific) to remove the His<sub>10</sub>-SUMO-tag from  $\sigma^{70}$ , followed by dialysis. Cleaved sample was further purified on a HiTrap IMAC HP column (GE Healthcare Life Sciences). Tagless  $\sigma^{70}$  was collected in the flowthrough and concentrated by centrifugal filtration. The sample was then loaded onto a HiLoad 16/60 Superdex 200 for purification by size exclusion chromatography. Purified  $\sigma^{70}$  was supplemented with glycerol to a final concentration of 20% (v/v), flash-frozen in liquid N<sub>2</sub>, and stored at –80°C.

*Eco* TraR was purified as described previously (Chen et al., 2019b). His<sub>10</sub>-SUMO-TraR plasmid was transformed into *Eco* BL21(DE3) (Novagen). Protein expression was induced with 1 mM IPTG for 3 hr at 37°C. Cells were harvested and lysed with a French Press (Avestin) at 4°C. The supernatant was loaded onto HiTrap IMAC HP columns (GE Healthcare Life Sciences) for purification by nickel affinity chromatography. Eluted TraR was cleaved with ULPI SUMO protease (Thermo Fisher Scientific) to remove the His<sub>10</sub>-SUMO-tag, followed by dialysis. Cleaved sample was further purified on a HiTrap IMAC HP column (GE Healthcare Life Sciences). Tagless TraR was collected in the flowthrough and concentrated by centrifugal filtration. The sample was loaded onto a HiLoad 16/60 Superdex 200 column (GE Healthcare Life Sciences) and purified by size exclusion chromatography. Purified TraR was concentrated by centrifugal filtration, flash-frozen in liquid N<sub>2</sub>, and stored at –80°C.

### Native mass spectrometry analysis

The RNAP holoenzyme (holo) was assembled by incubating RNAP core and  $\sigma^{70}$  (1:1.3 molar ratio) at room temperature (RT) for 10 min. TraR was then added at five-fold molar excess to an aliquot of the RNAP holo and incubated at RT for 10 min. The resulting samples (RNAP holo with and without TraR) were concentrated using Amicon Ultra 0.5-mL centrifugal filters (EMD Millipore, Burlington, MA) with a 100 kDa molecular weight cutoff (MWCO).

The samples were buffer-exchanged into native MS solution (150 mM ammonium acetate, pH 7.5, 0.01% Tween-20) using Zeba microspin desalting columns (Thermo Fisher Scientific, Waltham, MA) with a 40-kDa MWCO (Olinares et al., 2016). The promoter DNA (*rpsT* P2: –60 to +25) was initially desalted into HPLC-grade H<sub>2</sub>O. Prior to mixing, the concentrations of the protein complex post-buffer exchange and the DNA components were determined using a NanoDrop spectrophotometer (Thermo Fisher Scientific). To assemble the protein-DNA complexes, the promoter DNA was mixed at 3.2- to 4-fold excess with the buffer-exchanged protein sample and incubated at RT for 10 min. The ammonium acetate concentration of the sample was varied from 75 mM to 300 mM to determine optimal conditions for complex assembly.

For native MS analysis, 2–3  $\mu$ L of sample was loaded into a gold-coated quartz emitter that was prepared in-house and then electrosprayed into an Exactive Plus EMR instrument (Thermo Fisher Scientific) with a static nanospray source. The typical MS parameters include: spray voltage, 1.0–1.4 kV; capillary temperature, 100°C – 150°C; in-source dissociation, 10 V; S-lens RF level, 200; resolving power, 8,750 or 17,500 at m/z of 200; AGC target,  $1 \times 10^6$ ; maximum injection time, 200 ms; number of microscans, 5; injection flatapole, 8 V; interflatapole, 4 V; bent flatapole, 4 V; high energy collision dissociation (HCD), 200 V; ultrahigh vacuum pressure,  $6\text{--}8 \times 10^{-10}$  mbar; total number of scans, at least 100. Mass calibration in EMR mode was performed using cesium iodide. The acquired MS spectra were visualized using Thermo Xcalibur Qual Browser (version 3.0.63) and deconvolution was performed either manually or using UniDec v 3.2 (Marty et al., 2015; Reid et al., 2019). The deconvolved spectra from UniDec were plotted using the m/z software (Proteometrics LLC, New York, NY). Experimental masses were reported as the average mass  $\pm$  standard deviation (SD) across all the calculated mass values obtained within the observed charge state distribution. The experimentally determined masses include: 470,745  $\pm$  15 Da (0.02% mass error) for the TraR-E $\sigma^{70}$  complex; 523,900  $\pm$  150 Da (0.16% mass error) for the TraR-E $\sigma^{70}$ -*rpsT* P2 complex; 462,740  $\pm$  25 Da (0.07% mass error) for E $\sigma^{70}$ ; 452,700  $\pm$  20 Da (0.09% mass error) for the E $\sigma^{70}$ - $\omega$  complex; 515,800  $\pm$  160 Da (0.2% mass error) for the E $\sigma^{70}$ -*rpsT* P2 complex.

### KMnO<sub>4</sub> and DNase I footprinting

Wt or T<sub>7</sub>A *rpsT* P2 promoter fragments were <sup>32</sup>P-3' end labeled in the nt-strand by linearizing 15  $\mu$ g of plasmid DNA by NheI digestion [pRLG11272, wt, (Gopalkrishnan et al., 2017); or pRLG12844, T<sub>7</sub>A], followed by incubation with  $\alpha$ -<sup>32</sup>P-dCTP (Perkin Elmer, Waltham, MA) and Sequenase Version 2.0 (Thermo Fisher Scientific). Promoter fragments were then generated by digestion with NcoI, purified by 5% acrylamide gel electrophoresis, eluted by diffusion and concentrated using a PCR Purification Kit (QIAGEN, Hilden, Germany) as described (Gopalkrishnan et al., 2017). For 3'-labeling of the t-strand, plasmid DNA was digested at the Nco I site, labeled, and fragments were generated by Nhe I digestion. Promoter complexes were formed by incubation for 10 min at the indicated temperatures with RNAP (20 nM) and TraR (1  $\mu$ M), where indicated, in 10 mM Tris-Cl, pH 8.0, 10 mM MgCl<sub>2</sub>, 1 mM DTT, 0.1 mg/ml BSA and 30 mM KCl. For KMnO<sub>4</sub> footprinting, complexes were incubated with 2 mM KMnO<sub>4</sub> for 30 s, then samples were ethanol precipitated twice, incubated with 1 M piperidine at 90°C for 30 min, ethanol precipitated and run on 9.5% acrylamide, 7 M urea gels as described (Winkelman et al., 2015). For DNase I footprinting, complexes were digested with DNase I (Worthington, Columbus, OH; 10  $\mu$ g/ml) for 30 s, phenol extracted, ethanol precipitated, resuspended and analyzed by gel electrophoresis as for KMnO<sub>4</sub> samples. Gels were

dried, visualized by phosphorimaging and quantified using ImageQuant 5.2 (GE Healthcare, Pittsburgh PA). RNAPs, wt or variant, were purified by overexpression in *Eco* BL21(DE3) from derivatives of the multisubunit RNAP plasmid pIA900 (Svetlov and Artsimovitch, 2015), or derivatives containing  $\beta$  or  $\beta'$  ( $\beta'\Delta 215-220$ : pRLG10030;  $\beta A474V$ : pRLG15444;  $\beta 474L$ , pRLG15445).

### **In vitro transcription assays**

*In vitro* transcription was carried out on supercoiled templates as described (Gopalkrishnan et al., 2017). Multiple-round *in vitro* transcription assays were performed on linear *rpsT* 2 fragments with  $-60/+25$  endpoints (Figures S1E and S1F). Transcription reactions (25  $\mu$ L) containing 40 nM DNA, TraR (0 - 2  $\mu$ M), 60 nM RNAP and NTPs (500  $\mu$ M CTP, 200  $\mu$ M GTP, 200  $\mu$ M ATP, 10  $\mu$ M UTP, 1  $\mu$ Ci [ $\alpha$ - $^{32}$ P] UTP) were incubated in buffer (10 mM Tris-HCl pH 7.9, 170 mM NaCl, 10 mM MgCl<sub>2</sub>, 1 mM DTT and 0.1  $\mu$ g/ $\mu$ L BSA) at room temperature ( $\sim 23^\circ\text{C}$ ) for 15 minutes and were terminated by addition of equal volume of stop solution. Transcripts were separated on 8% acrylamide-7M urea denaturing gels and analyzed by phosphorimaging.

### **Preparation of TraR-RNAP-DNA complexes for Cryo-EM**

RNAP holo was formed by mixing RNAP core and a 2-fold molar excess of  $\sigma^{70}$  and incubating for 15 minutes at RT. RNAP holo was purified over a Superose 6 Increase 10/300 GL column (GE Healthcare, Pittsburgh, PA) in gel filtration buffer (10 mM Tris-HCl, pH 8.0, 200 mM KCl, 5 mM MgCl<sub>2</sub>, 10  $\mu$ M ZnCl<sub>2</sub>, 2.5 mM DTT). The eluted RNAP holo was concentrated to  $\sim 10.0$  mg/mL ( $\sim 20$   $\mu$ M) by centrifugal filtration (Amicon Ultra). TraR was added (5-fold molar excess over RNAP) and the sample was incubated for 15 min at RT. Duplex *rpsT* P2 promoter fragment ( $-60$  to  $+25$ , Integrated DNA Technologies, Coralville, IA), either wild-type (Figure 1A) or *rpsT* P2\* (Figure 2A), was added to the concentrated TraR-RNAP to 3-fold molar excess. The sample was incubated for 20 min at RT prior to cryo-EM grid preparation.

### **Cryo-EM grid preparation**

CHAPSO {3-[(3-cholamidopropyl)dimethylammonio]-2-hydroxy-1-propanesulfonate} (Anatrace, Maumee, OH) was added to the samples to a final concentration of 8 mM (Chen et al., 2019a). The final buffer condition for all the cryo-EM samples was 10 mM Tris-HCl, pH 8.0, 100 mM KCl, 5 mM MgCl<sub>2</sub>, 10  $\mu$ M ZnCl<sub>2</sub>, 2.5 mM DTT, 8 mM CHAPSO. C-flat holey carbon grids (CF-1.2/1.3-4Au, Protochips, Morrisville, NC) were glow-discharged for 20 s prior to the application of 3.5  $\mu$ L of the samples. Using a Vitrobot Mark IV (Thermo Fisher Scientific Electron Microscopy, Hillsboro, OR), grids were blotted and plunge-froze into liquid ethane with 100% chamber humidity at  $22^\circ\text{C}$ .

### **Cryo-EM data acquisition and processing**

#### **TraR-RNAP-wt-*rpsT* P2 complexes**

Grids were imaged using a 300 keV Titan Krios (Thermo Fisher Scientific Electron Microscopy) equipped with a K2 Summit direct electron detector (Gatan, Pleasanton, CA). Images were recorded with Serial EM (Mastrorarde, 2005) with a pixel size of 1.3  $\text{\AA}$  over a defocus range of  $-0.5$   $\mu\text{m}$  to  $-3.0$   $\mu\text{m}$ . Movies were recorded in super-resolution mode at 8 electrons/physical pixel/s in dose-fractionation mode with subframes of 0.2 s over a 10 s exposure (50 frames) to give a total dose of 80 electrons/physical pixel. Dose-fractionated movies were gain-normalized, drift-corrected, binned, summed, and dose-weighted using MotionCor2 (Zheng et al., 2017). The contrast transfer function was estimated for each summed image using Gctf (Zhang, 2016). Gautomatch (developed by K. Zhang, MRC Laboratory of Molecular Biology, Cambridge, UK, <https://www.mrc-lmb.cam.ac.uk/kzhang/Gautomatch>) was used to pick particles with an auto-generated template. Picked particles were extracted from the dose-weighted images in RELION (Scheres, 2012) using a box size of 256 pixels. The TraR-RNAP-wt-*rpsT* P2 dataset consisted of 5,330 motion-corrected images with 1,189,185 particles (Figure S2). A subset of the particles were used to generate an initial model of the complex in cryoSPARC (*ab initio* reconstruction) (Punjani et al., 2017) to generate a 3D template for RELION. In RELION, a consensus refinement was performed using the extracted particles and the cryoSPARC-generated initial model resulting in a 5.5  $\text{\AA}$  map (Figure S2). Using the refinement parameters, 3D classification ( $N = 2$ ) was performed on the particles without alignment, revealing a high resolution class with 370,441 particles (nominal resolution 3.9  $\text{\AA}$ ) after RELION 3D auto-refinement and a low-resolution 'junk' class that could not be classified further. Using the refinement parameters, a subsequent 3D classification ( $N = 2$ ) was performed on the high-resolution particles without alignment, revealing distinct classes with different DNA configurations: Class 1a contained duplex DNA bound to RNAP while class 1b contained a transcription bubble. Subsequent 3D masked classification ( $N = 2$ , without alignment) was performed on particles from class 1a using a mask around the downstream DNA,  $\beta$  protrusion, and  $\sigma^{70}_2$ . Classification revealed two distinct classes: TRPc and TRPi1 (Figure S2). Using the refinement parameters, subtractive 3D classification ( $N = 3$ ) was performed on the particles from class 1b by subtracting density outside of TraR,  $\beta$ lobe-Si1,  $\beta'$ Si3, and the downstream channel, followed by classifying the remaining density with a mask. Classification revealed three distinct classes: TRPi2, TpreRPo and TRPo (Figure S2). After 3D classifications, the particles within each class were further processed using RELION CTF refinement and Bayesian Polishing. RELION 3D auto-refinement and post-processing of the polished particles resulted in structures with the following nominal resolutions: TRPc (3.4  $\text{\AA}$ ), TRPi1 (3.4  $\text{\AA}$ ), TRPi2 (3.9  $\text{\AA}$ ), TpreRPo (3.5  $\text{\AA}$ ), TRPo (3.7  $\text{\AA}$ ). Local resolution calculations were generated using blocres and blocfilt from the Bsoft package (Cardone et al., 2013).

### **TraR-RNAP-rpsT P2\* complexes**

Grids were imaged as for the TraR-RNAP-wt-rpsT P2 dataset with the following exceptions: 1) The defocus range was  $-0.5 \mu\text{m}$  to  $-2.0 \mu\text{m}$ . Data were collected with a dose of 5.6 electrons/pixel/s. Images were recorded over a 15 s exposure using 0.3 s subframes (50 total frames) to give a total dose of 84 electrons/physical pixel. Dose-fractionated subframes were gain-normalized, drift-corrected, binned, summed, and dose-weighted using MotionCor2 (Zheng et al., 2017) in RELION 3.0 (Zivanov et al., 2018). The contrast transfer function was estimated for each summed image using CTFFIND4 (Rohou and Grigorieff, 2015). The TraR-RNAP-rpsT P2\* dataset consisted of 1,500 motion-corrected images with 523,503 particles (Figure S5A). A subset of the particles was subjected to cryoSPARC *ab initio* reconstruction (Punjani et al., 2017) to generate a 3D template for RELION refinements and classifications. In RELION, 3D classification ( $N = 2$ ) was performed on the extracted particles with alignment to the cryoSPARC *ab initio* reconstruction. Classification revealed a low-resolution class and a high-resolution class containing 150,387 particles with nominal resolution of 4.6 Å after RELION 3D auto-refinement. Refinement metadata and post-processing were used as inputs for RELION CTF refinement and RELION Bayesian Polishing (Zivanov et al., 2018). Polishing improved the map to a nominal resolution of 3.1 Å after RELION 3D auto-refinement. Using the refinement parameters, subtractive 3D classification ( $N = 3$ ) was performed on the polished particles by subtracting density outside of  $\sigma^{70}_{1,1}$ ,  $\sigma^{70}_2$ ,  $\beta$ -lobe,  $\beta$ -protrusion, and downstream DNA, followed by a 3D classification of the remaining density with a mask. This classification revealed two distinct classes: TRPi1.5a (class2a) and TRPi1.5b (class 2b and class 2c combined; Figure S5A). Particles from the TRPi1.5a class were further processed using RELION CTF refinement and RELION Bayesian Polishing, resulting in an improved map with a nominal resolution of 3.5 Å after RELION 3D auto-refinement and post-processing. RELION CTF refinement and RELION Bayesian Polishing did not improve the resolution of the TRPi1.5b class (nominal resolution of 3.0 Å after RELION 3D auto-refinement and post-processing).

### **Model building and refinement**

For initial models of the complexes, the TraR-RNAP structure (PDB ID 6N57) (Chen et al., 2019b) was manually fit into the cryo-EM density maps using Chimera (Pettersen et al., 2004) and real-space refined using Phenix (Adams et al., 2010). The DNAs were mostly built *de novo* based on the density maps. For real-space refinement, rigid body refinement with sixteen manually-defined mobile domains was followed by all-atom and B-factor refinement with Ramachandran and secondary structure restraints. Refined models were inspected and modified in Coot (Emsley and Cowtan, 2004).

### **QUANTIFICATION AND STATISTICAL ANALYSIS**

The nMS spectra were visualized using Thermo Xcalibur Qual Browser (version 3.0.63), deconvolved using UniDec v 3.2 (Marty et al., 2015; Reid et al., 2019) and plotted using the m/z software (Proteometrics LLC, New York, NY). Experimental masses (Figures 1B, S1C, and nMS analysis section on Method Details) were reported as the average mass  $\pm$  standard deviation across all the calculated mass values obtained within the observed charge state distribution.

ImageQuant 5.2 (GE Healthcare, Pittsburgh PA) was used to visualize and quantify gels. To quantify the transcription assays (Figures 5E, S1F, S1E, and S7E–S7H), mean values and the standard error of the mean from at least three independent measurements were calculated.

Structural biology software was accessed through the SBGrid consortium (Morin et al., 2013). The local resolution of the cryo-EM maps (Figures S3C–S3G, S5G, and S5H) was estimated using blocres (Cardone et al., 2013) with the following parameters: box size 15, verbose 7, sampling 1.3, and cutoff 0.5. The quantification and statistical analyses for model refinement and validation were generated using MolProbity (Chen et al., 2010) and PHENIX (Adams et al., 2010).

### **DATA AND CODE AVAILABILITY**

The cryo-EM density maps have been deposited in the EMDDataBank under accession codes EMD-20460 (TRPc), EMD-20461 (TPRi1), EMD\_20462 (TRPi1.5a), EMD-20463 (TRPi1.5b), EMD-20464 (TRPi2), EMD-20465 (TpreRPo), and EMD-20466 (TRPo). The atomic coordinates have been deposited in the Protein Data Bank under accession codes PDB: 6PSQ (TRPc), 6PSR (TRPi1), 6PSS (TRPi1.5a), 6PST (TRPi1.5b), 6PSU (TRPi2), 6PSV (TpreRPo), and 6PSW (TRPo).